学位論文（要約）

Hydrodynamic escape of mineral atmosphere on hot rocky exoplanet: impacts on the evolution of planetary mass and atmospheric composition

（主星近傍をまわる岩石系外惑星のミネラル大気の流体力学的散逸：惑星質量及び大気組成の進化への影響）

平成29年12月博士（理学）申請

東京大学大学院理学系研究科
地球惑星科学専攻
伊藤祐一

Abstract

Exoplanet surveys over the past two decades have revealed that there are a variety of planets beyond the Solar system (called exoplanets) and detected a growing number of small-size exoplanets of 1 to 2 Earth radii (often called super-Earths). Many of those small-size exoplanets are expected to be rocky planets. In contrast to the terrestrial planets in the Solar system, some of them are in environments hot enough that their surface temperatures are higher than the melting/vaporization temperature of rock. Such exoplanets are called hot rocky exoplanets in this study. Thus, hot rocky exoplanets likely have global magma oceans and also atmospheres that are composed of gases vaporized from the magmas. These atmospheres are called mineral atmospheres in this study. At present, we are expected to move into a new era of characterizing the atmosphere of hot rocky exoplanets, thanks to near-future space telescopes such as James Webb Space Telescope (JWST). Such characterization is crucially important to know not only what they are like but also how they were formed. Also, recent observations reported on the detection of close-in exoplanets with dusty tails and hot rocky exoplanets with extended sodium atmospheres, suggesting that there are rocky planets currently evaporating and losing parts of their masses. However, if this is the case, it is puzzling why many hot rocky super-Earths currently detected could have survived such evaporative mass loss.

Towards linking the current state of hot rocky exoplanets to their formation, it is necessary to understand their evolution. In particular, the escape of planetary atmospheres is one of the most important processes that change the mass and bulk composition of close-in planets extremely irradiated by stellar UV. The purpose of this study is to investigate the hydrodynamic escape of the mineral atmosphere, for which there are no theoretical studies, considering the details of the elementary processes involved, and derive the mass loss rate via that hydrodynamic escape.

I have developed my own hydrodynamic code for simulating the one-dimensional (along the line connecting the planetary and stellar centers), steady hydrodynamic motion of the highly XUV-irradiated atmosphere that is in the chemical equilibrium with the magma ocean at its bottom. Also, for considering the energy budget in the atmosphere in detail, I have taken into account photo- and thermo-chemistry, non-LTE radiative/chemical processes for heating and cooling, thermal conduction, and multi-component ambipolar diffusion of Na, O, Si, Mg, their multiple-charged ions and electrons, which are the major components in the mineral atmosphere. The magma ocean is assumed to be free of volatile and its composition is that of the bulk-silicate Earth (BSE). Also, the planet is assumed to be orbiting at 0.02 AU around a young Sun-like

star. I have investigated the dependence of the hydrodynamic escape on planetary gravity and on stellar XUV flux through the simulations for three different planetary masses, namely 10, 1, and 0.1 $M_\oplus$ and two different stellar ages, namely 0.1 and 1 Gyr.

I have found the two regimes of the hydrodynamic escape of the mineral atmosphere. One is the regime that I call the *global-cooling-limited* escape. This occurs on hot rocky exoplanets with high gravity such as the super-Earth-mass (10 $M_\oplus$) and Earth-mass (1 $M_\oplus$) cases. As the dominant process in this escape regime, almost all of the incident XUV energy from the host-star is converted into the radiative emission due to electronic transition in Na, Mg^+, Si^{2+}, Na^{3+} and Si^{3+}. The mass loss rates that I have derived in the 10 $M_\oplus$ and 1 $M_\oplus$ cases are relatively low, but massive enough for the atmosphere to remove completely the major species Na. For instance, the mass loss rate is on the order of 10^{-2} $M_\oplus$/Gyr for the 10 $M_\oplus$ case at the stellar age of 0.1 Gyr. And the mass loss rate increases linearly with incident stellar XUV flux. The other is the regime that I call the *FUV-and-visible-energy-limited* escape. In this escape regime, I have found that the mass loss rate is massive enough to lose all the planetary mass. This is because not only the FUV energy but also the visible light energy from the host star is used to efficiently drive the atmospheric motion. This occurs on hot rocky exoplanets with low gravity such as the 0.1 $M_\oplus$ case. The estimated mass loss rates are as high as 4.9×10^2 $M_\oplus$/Gyr and 5.1×10^2 $M_\oplus$/Gyr for the stellar ages of 0.1 and 1 Gyr, respectively; the mass loss rate is found to be independent of stellar XUV flux. Thus, in the present study, I have demonstrated that hot rocky exoplanets of 0.1 $M_\oplus$ selectively evaporate through the hydrodynamic escape of the mineral atmospheres, but ones of ≥ 1 $M_\oplus$ survive. It has been demonstrated that consideration of atmospheric escape is crucial for understanding the current state and origin of close-in rocky exoplanets.

Contents

Chapter 1

Introduction

本章については、5年以内に雑誌等で刊行予定のため、非公開。

Chapter 2

Review of hydrostatic solution of mineral atmosphere

In this chapter, I review our previous study (Ito et al. 2015), in order to show the composition and temperature structure of a mineral atmosphere in hydrostatic equilibrium. This study estimates the hydrostatic solution and the detectability of the emission spectra of a mineral atmosphere, theoretically. In particular, of special interest in Ito et al. (2015) are rocky super-Earths with masses of $\leq 10M_{\oplus}$ and radii of $\leq 2R_{\oplus}$ that are orbiting so close to their host stars that their surface temperatures are above the vaporization temperature of rock, because of intense stellar irradiation. Such exoplanets are referred to as HRSE.

The composition of the atmosphere is obtained numerically in section 2.1. Also, we compile the absorption line data for the major gas species, which are published in the literature or online, and then calculate the absorption opacities in section 2.2. Using the chemical compositions and absorption opacities, we integrate the thermal structure of the irradiated atmosphere in radiative, chemical and hydrostatic equilibrium in section 2.3. Then, we evaluate the detectability of the chemical species in the mineral atmosphere through the emission spectra obtained during secondary eclipse in section 2.4.

2.1 CHEMICAL COMPOSITION

2.1.1 Element abundance and gas pressure

To calculate the element abundance and pressure of gas in gas/melt chemical equilibrium with silicate melt for a given temperature, we use the chemical equilibrium code MELTS (Ghiorso & Sack 1995, Asimov & Ghiorso 1998), which performs the free-energy minimization calculations. Figures 2.1 and 2.2 show the calculated total pressures and molar fractions of gas species, respectively, over a temperature range between 1500 and 3000 K for four magma compositions such as (a) BSE, (b) the Earth's mid-ocean ridge basalts (MORB), (c) the Earth's bulk crust,

and (d) the Earth's upper crust. The detail of the magma compositions is shown in Table 2.1. In Ito et al. (2015), we consider the above four compositions of magma, following Schaefer & Fegley (2009), although the magma composition of exoplanets is uncertain. The actual magma composition depends not only on the element abundances but on the thermal history of the planet; exploring the details is beyond the scope of Ito et al. (2015). Note that the choice among the four magma compositions has little impact on the emission spectra in the infra-red wavelength region.

The overall trend shown in Figs. 2.1 and 2.2 is similar with that found by Schaefer & Fegley (2009) and Miguel et al. (2011), who used the MAGMA chemical equilibrium code (Fegley & Cameron 1987), instead of MELTS. For example, Na is the most abundant species in most of the temperature range, while SiO increases with temperature and becomes the most abundant one for $T \gtrsim 2800$ K for BSE and MORB, $T \gtrsim 2600$ K for the bulk crust, and $T \gtrsim 2500$ K for the upper crust. Also, the total vapor pressure is as small as $\sim 10^{-7}$ bar at $T = 1500$ K and ~ 0.1 bar at $T = 3000$ K, for example (see Fig. 2.1).

A noticeable difference is seen in the abundance of potassium gas between our calculations and those by Schaefer & Fegley (2009) and Miguel et al. (2011). Our calculations yield much higher partial pressure of potassium: The ratio of the potassium to sodium partial pressures that we have obtained is larger by a factor of more than 100, relative to that calculated by Schaefer & Fegley (2009). This difference is due mainly to that in the adopted thermodynamic model for silicate melt. The melt model of MAGMA used in Schaefer & Fegley (2009) is ideal mixing of many simple and complex fictitious oxide species, which is calibrated for silicate melts with high-K_2O contents, whereas MELTS used in Ito et al. (2015) adopts a symmetric regular solution model with minimum melt components, which is calibrated by experimental results on natural systems with low-K_2O abundances. MAGMA would appropriately estimate potassium vapor pressure for high-K_2O melt as shown in Fig. 5 of Schaefer & Fegley (2004), but is not good for low-K_2O melt. By contrast, MELTS gives appropriate results for low-K_2O melt, which is of interest in Ito et al. (2015) (see Table 2.1). The impact on the emission spectrum from the mineral atmosphere is discussed in section 6.6 of Ito et al. (2015).

Table 2.1: Bulk compositions considered in Ito et al. (2015)

Oxide(wt%)	BSE[1]	MORB[1]	Bulk crust[2]	Upper crust[2]
SiO_2	45.1	49.6	60.6	66.6
MgO	37.9	9.75	4.70	2.50
FeO	8.06	8.06	6.71	5.04
Al_2O_3	4.46	16.8	15.9	15.4
CaO	3.55	12.5	6.41	3.59
Na_2O	0.36	2.18	3.07	3.27
Cr_2O_3	0.38	0.07	0.0004	0.0003
TiO_2	0.20	0.9	0.72	0.64
K_2O	0.03	0.07	1.81	2.80
P_2O_5	0.02	0.10	0.13	0.15

Notes. [1]McDonough & Sun (1995), [2]Rudnick & Gao (2003)

2.1.2 Gas phase equilibrium

To calculate the equilibrium abundances of gas species in the mineral atmosphere, we use the NASA CEA code (Gordon & McBride 1996), which performs the free-energy minimization calculations. In practice, we calculate the abundances for some selected temperatures from 2000 K to 4500 K and pressures from 10^{-8} bar to 10^{-1} bar, which are of interest in Ito et al. (2015), considering the gas phase equilibrium of a system composed of only the major elements such as O, Na, K, Si and Fe. We assume that the element abundances are vertically constant; their values are calculated in section 2.1.1.

In our atmosphere model, the molar fractions of Na, K and Fe gas vary little, compared to those of O, O_2, Si and SiO. O_2 and SiO tend to decrease and O and Si increase with altitude in low pressure regions in the atmosphere (see section 2.3), because of thermal dissociations of O_2 and SiO.

Although we ignore photo-chemical reactions in Ito et al. (2015), the photo-dissociation of SiO may be important for the detectability of the atmosphere. We discuss the possibility of the photo-dissociation of SiO and the impact on the atmospheric structure and detectability in section 6.3 of Ito et al. (2015).

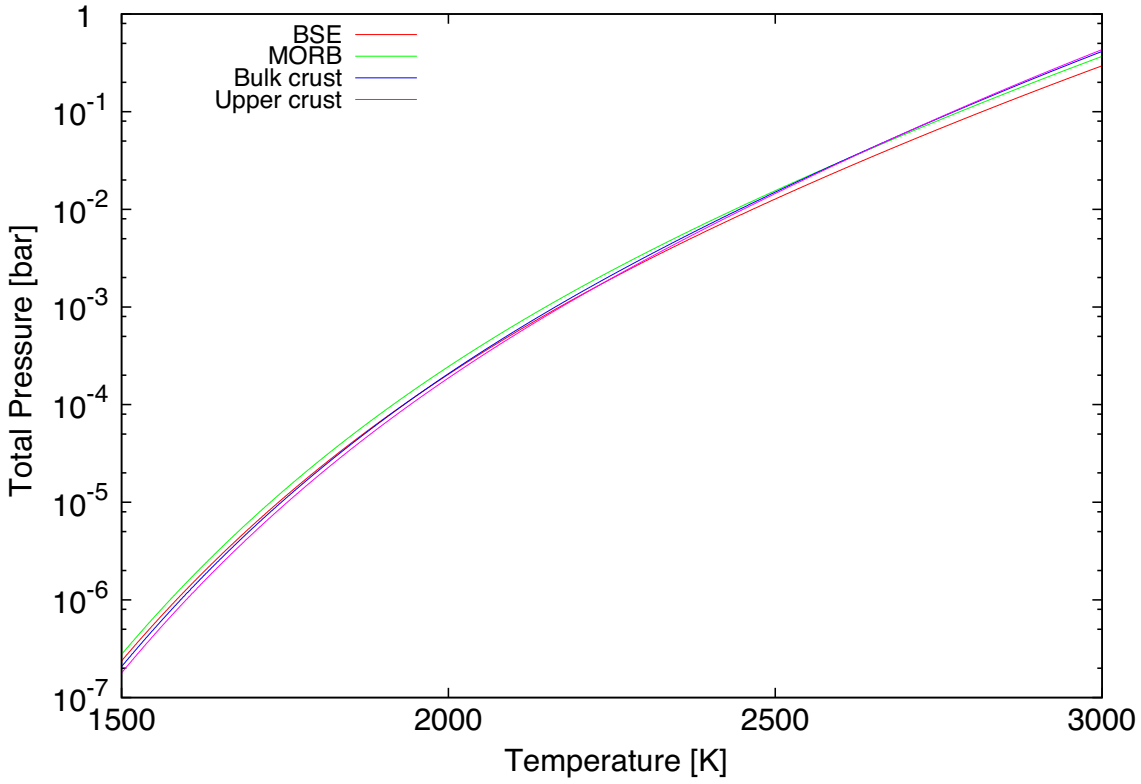

Figure 2.1: Total pressures of gas in gas/melt equilibrium with magma of assumed composition are shown as functions of temperature. The assumed bulk compositions are the same as those of the bulk silicate Earth (BSE) (red), the Earth's mid-ocean ridge basalts (MORB) (green), the Earth's bulk crust (blue), and the Earth's upper crust (magenta) (see Table 2.1 for the details).

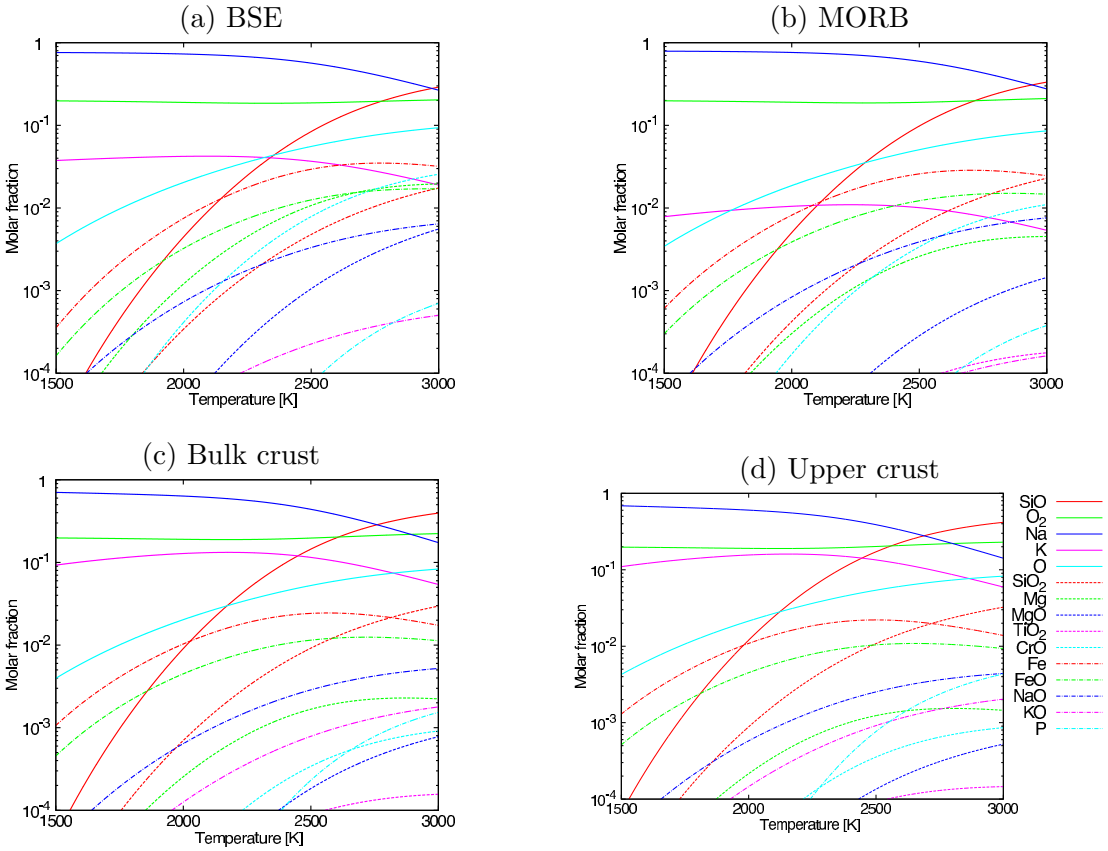

Figure 2.2: Composition of gas in chemical equilibrium with molten silicate. Molar fractions of the gas species are shown as functions of temperature. The assumed bulk compositions are the same as those of (a) the bulk silicate Earth (BSE), (b) the Earth's mid-ocean ridge basalts (MORB), (c) the Earth's bulk crust, and (d) the Earth's upper crust (see Table 2.1 for the details).

2.2 ABSORPTION OPACITY

Among the chemical species shown in Figure 2.2, we consider line absorption by seven major species that include Na, K, Fe, O, O_2, Si and SiO. We neglect Rayleigh scattering, because the Rayleigh scattering opacities are mostly smaller than the absorption opacity of SiO at wavelengths of interest in Ito et al. (2015), as discussed in section 6.1 of Ito et al. (2015) Note that while TiO is known to be a strong absorber for visible ray (Allard et al. 2000, Plez 1998), its absorption opacity is always smaller than Na absorption opacity in the visible and IR wavelength regions, because the molar fraction of TiO is negligibly small (e.g., $\sim 10^{-12}$ at $T = 1500$ K and $\sim 10^{-6}$ at $T = 3000$ K), compared to that of Na ($\gtrsim 0.1$) in the atmosphere considered here.

Absorption opacities are calculated in the following way, except for O_2, for which we apply vibrational-rotational transitions in the HITRAN database (Rothman et al. 2013). In local thermodynamic equilibrium, the absorption cross section of species A for an energy transition from the ith level to the jth level, $\sigma_\nu^{\rm A}(i,j)$, is given as (Piskunov & Kupka 2001)

$$\begin{aligned}\sigma_\nu^{\rm A}(i,j) =& g_i f_{ij} \frac{\pi e^2}{m_e c} \frac{\exp(-E_i/kT)}{Q(T)} \\ & \times \left\{ 1 - \exp\left(\frac{E_j - E_i}{k_b T} \right) \right\} H(\nu, a), \end{aligned} \tag{2.1}$$

where ν is the frequency, g_i is the statistical weight of the ith energy level, f_{ij} is the oscillator strength for a transition from the ith (lower) to jth (higher) level, E_i and E_j are excitation energies of the ith and jth energy levels, respectively, and $Q(T)$ is the partition function of the species at temperature T. e is the elementary charge ($= 4.803 \times 10^{-10}$ esu), m_e is the electron mass ($= 9.1094 \times 10^{-28}$ g), c is the light velocity ($= 2.9979246 \times 10^{10}$ cm s^{-1}), and k_b is the Boltzmann constant ($= 1.3806488 \times 10^{-16}$ erg K^{-1}). We take the values of g_i, f_{ij} and E_i from Kurucz (1992) (see also Barton et al. (2013) for SiO). Also we take the values of $Q(T)$ for Na, K, Fe, Si and O from Irwin (1981) and for SiO from Rossi et al. (1985).

The function $H(\nu, a)$ is the line profile function given by (e.g., Rybicki & Lightman 1986)

$$H(\nu, a) = \frac{V(\nu, a)}{\sqrt{\pi} \Delta\nu_D}, \tag{2.2}$$

where a is the line width parameter, $V(\nu, a)$ is the Voigt function, and $\Delta\nu_D$ is the Doppler width given by

$$\Delta\nu_D = \frac{\nu_0}{c} \sqrt{\frac{2kT}{m_A}}, \tag{2.3}$$

where m_A is the mass of the absorber and ν_0 is the central frequency of the spectral line. The line width parameter a is calculated with damping constants for natural broadening and van

der Waals broadening as (Piskunov & Kupka 2001)

$$a = \frac{\Gamma_r + \Gamma_W}{4\pi\Delta\nu_D}. \tag{2.4}$$

According to Unsold (1955) and Gray (1976), Γ_r and Γ_W are given by

$$\Gamma_r = 0.222 \times 10^{14}\lambda^{-2}, \tag{2.5}$$

$$\Gamma_W = 17 \times \left(0.3 \times 10^{-30}\left[\frac{(l+1)^2}{(I-\chi_j)^2} - \frac{(l+1)^2}{(I-\chi_i)^2}\right]\right)^{2/5} \times v^{3/5}N, \tag{2.6}$$

where λ is wavelength in nm, N is the total number density of the gas species in cm^{-3}, I is the ionization potential in eV, χ_i is the excitation potential at the ith level in eV, and l is the electric charge. v is the relative thermal velocity defined by

$$v = v^A\sqrt{1 + \frac{\mu^A}{\overline{\mu}}}, \tag{2.7}$$

where v^A is the thermal velocity of the absorber and μ^A and $\overline{\mu}$ are the molecular weight of the absorber and the mean molecular weight, respectively. As for the SiO absorption opacity, we assume $\Gamma_W = 10^{-7} \times N$, following Kurucz & Avrett (1981). To calculate the line profile $H(\nu, a)$ numerically, we use a polynomial expansion of the Voigt function given by Kuntz (1997). We have confirmed that this approximation yields relative errors of the order of 10^{-4}, which is small enough for our discussion in Ito et al. (2015).

Figure 2.3 shows the cross section of each species multiplied by each molar fraction as a function of wavelength for $T = 2000$ K(a) and 3000 K(b), respectively. The assumed pressures are 1.0×10^{-5} bar for $T = 2000$ K and 0.01 bar for $T = 3000$ K. The magma composition is assumed to be BSE. The calculated molar fractions of Na, K, Fe, Si, SiO, O, and O_2 are, respectively, $x_{\mathrm{Na}} = 0.721$, $x_{\mathrm{K}} = 0.0407$, $x_{\mathrm{Fe}} = 0.001$, $x_{\mathrm{Si}} = 10^{-6}$, $x_{\mathrm{SiO}} = 0.00731$, $x_{\mathrm{O}} = 0.0233$, and $x_{\mathrm{O}_2} = 0.189$ for $T = 2000$ K(a) and $x_{\mathrm{Na}} = 0.204$, $x_{\mathrm{K}} = 0.0142$, $x_{\mathrm{Fe}} = 0.01$, $x_{\mathrm{Si}} = 1 \times 10^{-3}$, $x_{\mathrm{SiO}} = 0.343$, $x_{\mathrm{O}} = 0.0991$, and $x_{\mathrm{O}_2} = 0.211$ for $T = 3000$ K(b).

In Fig. 2.3a, the most abundant species Na (blue) presents a few hundred of strong absorption lines between 0.253 and 10.0 μm, including the D line at 0.5893 μm. Also, several hundred strong lines of K (magenta) that are distinguishable from the Na lines are also found between 0.286 and 10.0 μm, including potassium doublet lines at 0.766 and 0.770 μm. While SiO (red) is less abundant by a factor of about 100 than Na, millions of its electron-transition absorption lines dominate in the FUV wavelength region (0.14 - 0.3 μm) and its absorption due to rotation-vibration transition dominates in several parts of the IR wavelength region, except narrow line

peaks of Na, K and Fe. The O electron-transition absorption (cyan) dominates between 0.10 and 0.13 μm. The several thousands lines of Fe (grey) dominates between 0.20 and 0.54 μm. Although O_2 (green) is the second most abundant species, its absorption is obscured by the other absorptions except at a narrow range around 30 μm. Also, the Si electron-transition absorption (yellow) is obscured by the SiO absorption in both Figs. 2.3a and 2.3b and presents many prominent absorption lines between 0.1 and 0.3 μm.

In the higher-T case shown in Fig. 2.3b, the SiO feature is more prominent. The electron-transition absorption in the FUV region is larger by about two orders of magnitude than that in Fig. 2.3a, because the molar fraction of SiO is larger by two orders of magnitude (see Fig. 2.2) and comparable with Na at 3000 K. The most remarkable difference in absorption feature between Fig. 2.3a and Fig. 2.3b is that the SiO rotation-vibration absorption dominates at all the wavelengths longer than about 3 μm, except several hundreds of narrow lines of Na and K. The rises in the peak values of SiO are due to the increase in abundance, while the enhancement of pressure broadening also contributes to the rises in absorption between those peaks.

Other minor species might contribute to the opacity. As for Mg and P present in Fig. 2.2, we have confirmed that the absorption opacities of these species are negligibly small relative to the SiO absorption opacity in most of the wavelength region of interest, except for narrow ranges between 0.1 and 0.15 μm. Absorption line data of the diatomic molecules other than SiO in Fig. 2.2 are unavailable, to our knowledge. Thus, we have ignored their contribution.

Finally, for integrating the thermal structure of the atmosphere in the next section, we use the total absorption opacity, κ_ν, calculated as

$$\rho\kappa_\nu = N \sum_{\mathrm{A}} x_{\mathrm{A}} \sigma_\nu^{\mathrm{A}}(i,j), \tag{2.8}$$

where ρ is the mass density.

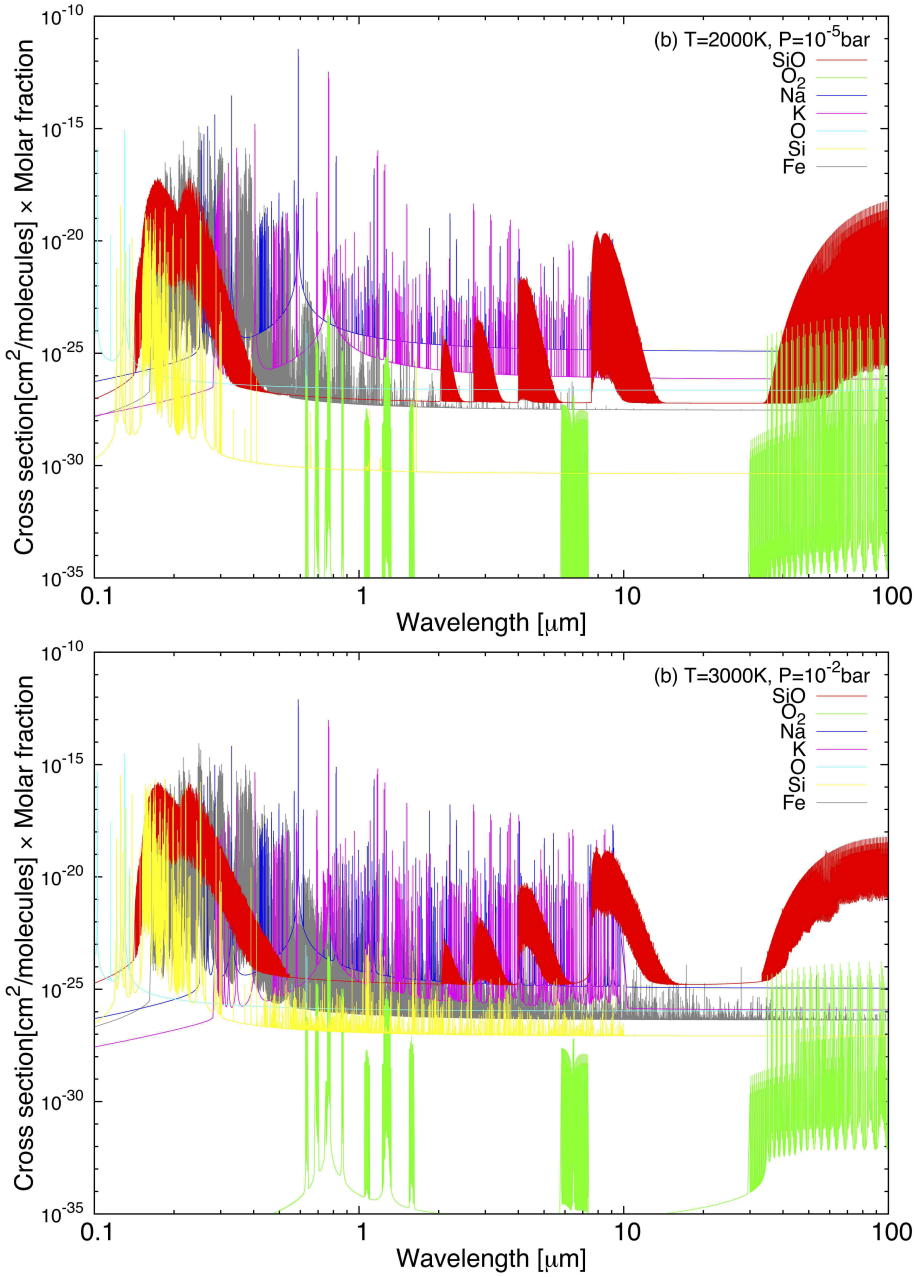

Figure 2.3: Absorption cross sections of the seven major gas species, SiO (red), O_2 (green), Na (blue), K (magenta), Fe (grey), O (cyan), and Si(yellow) as functions of wavelength. Each cross section is multiplied by each molar fraction. The magma composition is assumed to be BSE (see Table 2.1). (a): The temperature is 2000 K and the pressure is 1×10^{-5} bar. The calculated molar fractions of Na, K, Fe, Si, SiO, O, and O_2 are 0.721, 0.0407, 0.001, 1×10^{-6}, 0.00731, 0.0233, and 0.189, respectively. (b): The temperature is 3000 K and the pressure is 1×10^{-2} bar. The calculated molar fractions of Na, K, Fe, Si, SiO, O, and O_2 are 0.204, 0.0142, 0.01, 1×10^{-3}, 0.343, 0.0991, and 0.211, respectively.

2.3 TEMPERATURE PROFILE

In Ito et al. (2015), we simulate the one-dimensional plane-parallel thermal structure of the atmosphere that is in the radiative, hydrostatic, and chemical equilibrium. To do so, we integrate the so-called two-stream equations with the assumption of quasi-isotropic radiation, adopting the $\delta-$Eddington approximation (Toon et al. 1989):

$$\frac{dF_\nu^+}{d\tau_\nu} = \frac{7}{4}F_\nu^+ + \frac{1}{4}F_\nu^- - 2\pi B_\nu(T), \tag{2.9}$$

$$\frac{dF_\nu^-}{d\tau_\nu} = -\frac{1}{4}F_\nu^+ - \frac{7}{4}F_\nu^- + 2\pi B_\nu(T), \tag{2.10}$$

where F_ν^+ and F_ν^- are the upward and downward radiative fluxes, respectively, $B_\nu(T)$ is the Planck function, and τ_ν is the optical depth defined by

$$\frac{d\tau_\nu}{dz} = -\kappa_\nu \rho, \tag{2.11}$$

where z is the altitude. In equations (2.9) and (2.10), we have assumed that the single-scattering albedo is 0, because absorption dominates scattering in most of the wavelength region of interest, as described above. The boundary conditions at the top and bottom of the atmosphere are respectively $F_\nu^- = 0$ and $F_\nu^+ = \pi B_\nu(T_{\rm g})$, where $T_{\rm g}$ is the ground temperature. To solve equations (2.9) and (2.10), we have used the widely-used algorithm developed by Toon et al. (1989). According to Toon et al. (1989), the error in the radiative fluxes caused by the two-stream approximation was typically less than 10%, which is small relative to uncertainties in physical properties of exoplanets.

The net radiative flux integrated over all frequencies is constant throughout the atmosphere in radiative equilibrium. For an irradiated atmosphere, the net radiative flux, $F_{{\rm net},\nu}$, is written as

$$F_{{\rm net},\nu}(\tau_\nu) = F_\nu^+(\tau_\nu) - F_\nu^-(\tau_\nu) - \mu_* F_\nu^* e^{-\tau_\nu/\mu_*}, \tag{2.12}$$

where F_ν^* is the incident stellar flux and μ_* is the cosine of the zenith angle of the incident stellar radiation. The radiative equilibrium condition is given as

$$\int_0^\infty F_{{\rm net},\nu}\, d\nu = F_0, \tag{2.13}$$

where F_0 is the constant flux. An HRSE is subject to tidal heating. Its strength depends on orbital and internal properties of the HRSE (Barnes et al. 2010). The detailed consideration of the tidal heating effect is beyond the scope of Ito et al. (2015) (a brief discussion is made in section 6.4 of Ito et al. 2015). In Ito et al. (2015), we assume $F_0 = 10$ W/m^2 for numerical

stability. For $F_0 < 10$ W/m^2, we have confirmed that choice of F_0 have little influence on the thermal structure of the atmosphere.

We consider a pressure range from 1×10^{-8} bar to the pressure at ground level, $P_{\rm g}$. Note that $P_{\rm g}$ is determined a posteriori, because $P_{\rm g}$ is the vapor pressure, which depends on the ground temperature, $T_{\rm g}$. Numerically, the atmosphere is vertically divided into 50 layers. The layers are prepared so that the size of each layer logarithmically increases with pressure. In addition, to integrate equations (2.9) and (2.10), we consider 100 spectral intervals in a frequency range between 1×10^{13} and 2×10^{15} s^{-1} such that the size of each interval logarithmically increases with frequency. We calculate the harmonic mean opacities using cross sections obtained in section 2.2. The calculation method of the mean opacities is described in Appendix of Ito et al. (2015).

To find the thermal structure of the atmosphere in radiative equilibrium and also in gas-melt chemical equilibrium with the underlying magma ocean, we need three iterative procedures. Firstly, to find the radiative-equilibrium solution for given opacities and molar fractions of atmospheric gases, we integrate the equation of energy conservation,

$$\frac{dT_n}{d\widetilde{t}} = \frac{dF_n}{dP_n}, \tag{2.14}$$

where $\widetilde{t}$ is a normalized time, T_n, P_n and F_n are the temperature, pressure, and net radiative flux in the nth layer, respectively. The integration is continued until $|F_n - F_0|/F_0$ becomes smaller than 1 % in all the layers.

Secondly, once we find the radiative-equilibrium solution, we calculate the opacities that are consistent with temperatures obtained above. In practice, to save memory and cpu time, we have prepared a numerical table in which the harmonic mean opacities in 100 spectral intervals are given as functions of T, $\log P$, and, the mean molecular weight, $\overline{\mu}$: The grids are prepared for T = 2000, 2500, 3000, 3500, 4000, and 4500 K, $\log(P/\mathrm{bar}) = -1$, -2, -3, -4, and -5, and $\overline{\mu} = 25$, 30, and 35. In the pressure range from 1×10^{-8} bar to 1×10^{-5} bar, we have ignored the pressure dependence of the opacity because $\Gamma_r > \Gamma_W$ in the range. Note that we have checked that the calculated flux differs by at most 5 %, even if a smaller table with T = 2000, 3000, and 4000 K, $\log(P/\mathrm{bar}) = -1$, -3, and -5, and $\overline{\mu} = 25$ and 35 is used. The convergence condition is that the temperature in each layer does not vary within less than 1 %.

Finally, we have to find the solution in which the atmosphere is in equilibrium with the underlying magma ocean at its bottom. The ground pressure $P_{\rm g}$ and molar fractions $x_{\rm A}$ are functions of the ground temperature $T_{\rm g}$ (see section 2.1). From equations (2.12) and (2.13), the

magma being assumed to be a blackbody, $T_{\rm g}$ is given as

$$\sigma T_{\rm g}^4 = F_0 + \int_0^\infty \left\{ F_{n,\nu}^-(P_{\rm g}) + \mu_* F_\nu^* e^{-\tau_{\nu,{\rm g}}/\mu_*} \right\} d\nu, \tag{2.15}$$

where σ is the Stefan-Boltzmann constant ($= 5.67 \times 10^{-8}{\rm W/m^2K^4}$) and $\tau_{\nu,{\rm g}}$ is the total optical depth of the atmosphere. We calculate $T_{\rm g}$ from Eq. (2.15) and then calculate $P_{\rm g}$ and $x_{\rm A}$. The gas chemical equilibrium composition in each layer, $x_{\rm A}$, is obtained by interpolating linearly the tabulated data made by the NASA CEA code. The grids are prepared for $T = 2000$, 2500, 3000, 3500, 4000, and 4500 K, $\log(P/{\rm bar}) = -1$, -2, -3, -4, -5, -6, -7 and -8, and $T_{\rm g}$ being every one kelvin from 1500K to 3000K. The convergence condition is that $T_{\rm g}$ and the temperature in each layer do not vary within less than 1 %.

Figure 2.4 shows the calculated temperature profiles for different substellar-point equilibrium temperatures defined by

$$T_{\rm eq}^4 = (1 - A_p)\frac{R_*^2}{D^2} T_*^4, \tag{2.16}$$

where R_* and T_* are respectively the radius and temperature of the host star, A_p is the planetary albedo, and D is the orbital distance of the planet. Five values of $T_{\rm eq}$ are chosen: $T_{\rm eq} = 1800$ K (black), 2000 K (cyan), 2300 K (blue), 2500 K (green), and 3000 K (red). The incident stellar flux is calculated as $F_\nu^* = T_{\rm eq}^4/T_*^4 \times \pi B_\nu(T_*)$. The solid lines represent the temperature profiles at $\mu_* = 1/2$ (i.e., day-side average). Also, the open and filled circles show the temperatures at the bottom of the atmosphere, $T_{\rm b}$, and at the ground, $T_{\rm g}$, respectively. Figure 2.5 shows the calculated molar fraction profiles of seven major species for the atmosphere structure shown in Fig. 2.4. Here we have assumed $g = 25$ m/s^2 and $A_p = 0$. The host star is assumed to emit blackbody radiation of 6000 K. The magma composition is assumed to be BSE.

The most remarkable feature of the temperature profiles in Fig. 2.4 is the thermal inversion structure in the cases of $T_{\rm eq} \geq 2300$ K. As found in section 2.2, the absorption is more significant in the UV and visible wavelength regions (0.1 to $\sim$1 μm) than in the IR region ($\sim$1 to 4 μm), mainly because of the strong UV-ray absorption by SiO and visible-light absorption by the doublet lines of Na and K. (Note that most of the absorption lines of Fe, Na and K are too narrow to contribute to the mean opacity.) This means that the absorption of the incident stellar radiation is stronger compared to the intrinsic planetary radiation, which results in thermal inversion for $P \geq 10^{-5}$bar. For $P \leq 10^{-5}$bar, the temperature decreases with decreasing pressure, because the dissociation of SiO occurs as shown in Figure 2.5, so that the UV-ray absorption by SiO becomes weak.

Not only the thermal inversion region extends but $T_{\rm g}$ increases, as $T_{\rm eq}$ increases. In the case of $T_{\rm eq} = 3000$ K, $T_{\rm g}$, is significantly smaller than $\mu_*^{1/4} T_{\rm eq}$. In contrast, $T_{\rm g} \simeq \mu_*^{1/4} T_{\rm eq}$ for low

$T_{\rm eq}$, because the atmosphere is so optically thin that the ground is directly heated by stellar irradiation. In the cases of $T_{\rm eq} \leq 2000$ K, the atmosphere is thus isothermal. Note that jumps in temperature between $T_{\rm b}$ and $T_{\rm g}$ are found in Figure 2.4. This is because those atmospheres are optical thin for the incident stellar flux and any heat transfer process except radiative transfer is not taken into account. Thus, in reality, the atmosphere is not exactly isothermal, because there should be a conductive region with steep temperature gradient near the ground. Such structure, however, has little impact on the emission spectra that we use when discussing the detectability of HSREs in secondary eclipse (see section 2.4).

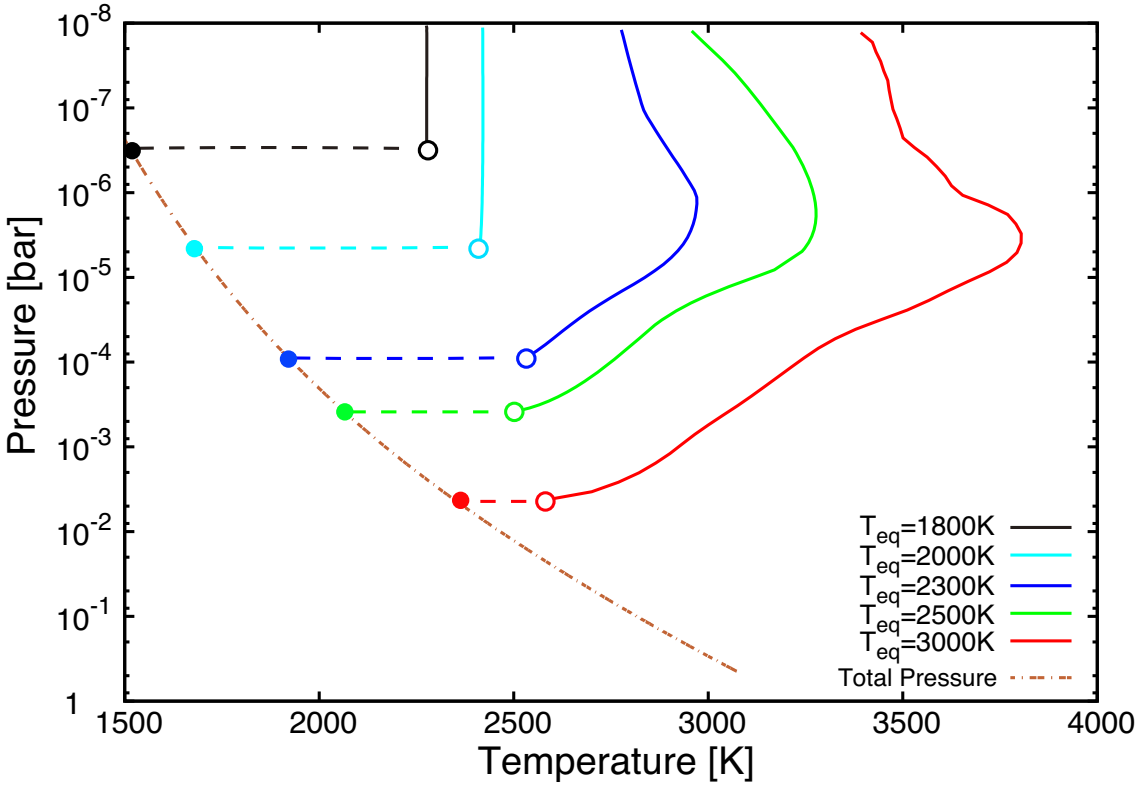

Figure 2.4: Temperature-pressure profile in the mineral atmosphere on top of the BSE magma of a super-Earth with gravity of 25 m/s^2 for five choices of the substellar-point equilibrium temperature, $T_{\rm eq}$, of 1800 K (black), 2000 K (cyan), 2300 K (blue), 2500 K (green), and 3000 K (red) (see eq. [2.16]; $A_p = 0$). The host star is assumed to be a Sun-like star with radius of 1 $R_\odot$ and effective temperature of 6000 K and emit the blackbody radiation of 6000 K. The solid lines show the day-side averaged profiles (i.e., the cosine of the stellar-light zenith angle $\mu_* = 1/2$; see eq. [2.12]). The open circles show the temperatures at the bottom of the atmosphere, $T_{\rm b}$, and the filled circles show the temperatures at the ground, $T_{\rm g}$. The orange dotted line represents the total vapor pressure for the BSE composition, which corresponds to the ground.

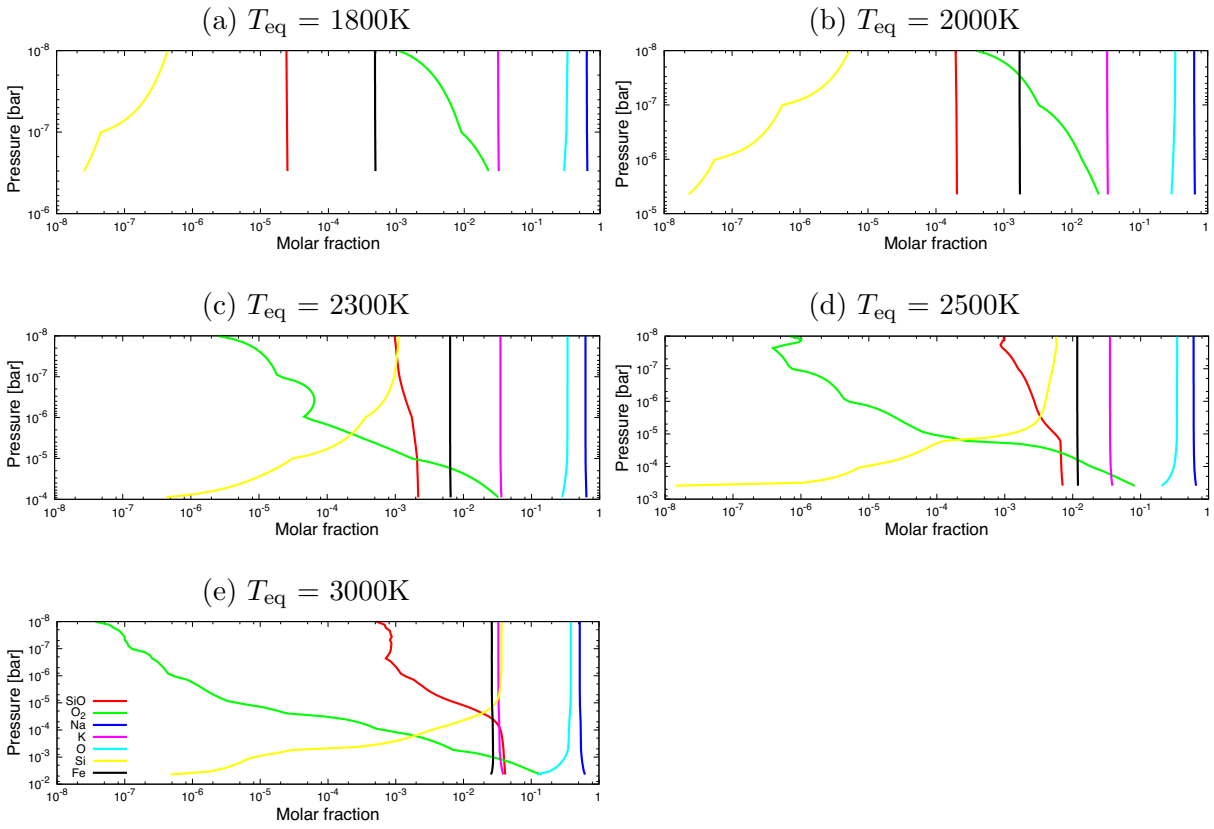

Figure 2.5: The distribution of the seven major gas species in chemical equilibrium in the mineral atmosphere. Molar fractions of SiO (red), O_2 (green), Na (blue), K (magenta), Fe (grey), O (cyan) and Si(yellow) are shown as functions of pressure for five choices of the substellar-point equilibrium temperature; (a) $T_{\rm eq}$ = 1800K, (b) 2000K, (c) 2300K, (d) 2500K, and (e) 3000K. The corresponding temperature-pressure structure of the atmosphere is shown in Figure 2.4.

2.4 DETECTABILITY VIA SECONDARY ECLIPSE OBSERVATION

2.4.1 Secondary eclipse depth

Here we assess the detectability of the mineral atmospheres of HRSEs that we have modeled via the secondary eclipse observation. This observation enables us to infer the vertical temperature profile and composition of an exoplanetary atmosphere by obtaining planetary emission spectrum. In particular, the thermal inversion structure found in section 2.3 is expected to be detected.

The secondary eclipse observation measures the ratio of the planetary luminosity to the sum of the stellar and planetary luminosities. The ratio is often called the secondary eclipse depth, ϵ_λ, which is given by

$$\epsilon_\lambda \simeq \left(\frac{R_p}{R_*}\right)^2 \frac{F_{p,\lambda} + A_p F_{*,\lambda}}{F_{*,\lambda}}, \tag{2.17}$$

where $F_{*,\lambda}$ is the emergent stellar flux and $F_{p,\lambda}$ is the emergent planetary flux calculated as

$$F_{p,\lambda} = \pi \int_0^\infty B_\lambda(T(\tau_\lambda)) e^{-\tau_\lambda} d\tau_\lambda. \tag{2.18}$$

Below, as in section 2.3, we assume $g = 25$ m/s^2, $A_p = 0$, and blackbody stellar radiation of 6000 K. The magma composition is assumed to be BSE. Also, we suppose an HRSE with radii of 2 $R_\oplus$ orbiting a solar analog, namely $R_p/R_* = 0.02$. To integrate equations (2.17) and (2.18), we consider 30000 spectral intervals in the wavelength range between 0.1 and 100 μm; the size of each interval logarithmically increases with wavelength. Then, as in section 2.3, we calculate the arithmetic mean opacities, interpolating linearly the tabulated data. We consider only the case of $\mu_* = 1/2$, because we are interested in planetary disk averaged emission (i.e., day-side average).

Figure 2.6 plots the secondary eclipse depth ϵ_λ (and also $F_{p,\lambda}/F_{*,\lambda}$) for $T_{\rm eq} = 1800$ K (black), 2000 K (cyan), 2300 K (blue), 2500 K (green), and 3000 K (red): Panels (a) and (b) show the spectra in the wavelength region of 0.1–100 μm and 0.3–1 μm, respectively. The secondary-eclipse-depth spectra for $T_{\rm eq} = 1800$ K and 2000 K exhibit only some narrow line features of Na and K. This is mainly because the atmospheres are isothermal (see Fig. 2.4) except for the temperature jump above the ground. The line features are, thus, due to the emission from parts of the atmosphere with temperatures higher than $T_{\rm g}$, while the continuous spectra are the black body spectra of $T_{\rm g}$.

By contrast, the spectra for $T_{\rm eq} = 2300$ K and 2500 K present noticeable features of SiO around 10 and 100 μm, in addition to hundreds of narrow features of Na and K. For $T_{\rm eq} =$

3000 K, a spectral feature by SiO around 4 μm appears in addition to those around 10 and 100 μm, as shown in the subfigure inside Fig.2.6a. The features of SiO become stronger as $T_{\rm eq}$ increases, because the SiO abundance is sensitive to temperature and also the thermal inversion is more significant at higher temperature. Additionally, one can also identify features of the sodium doublet at 0.589 μm and the potassium doublet at 0.77 μm and narrow line features of Fe, Na and K in the visible band, as shown in Panel (b).

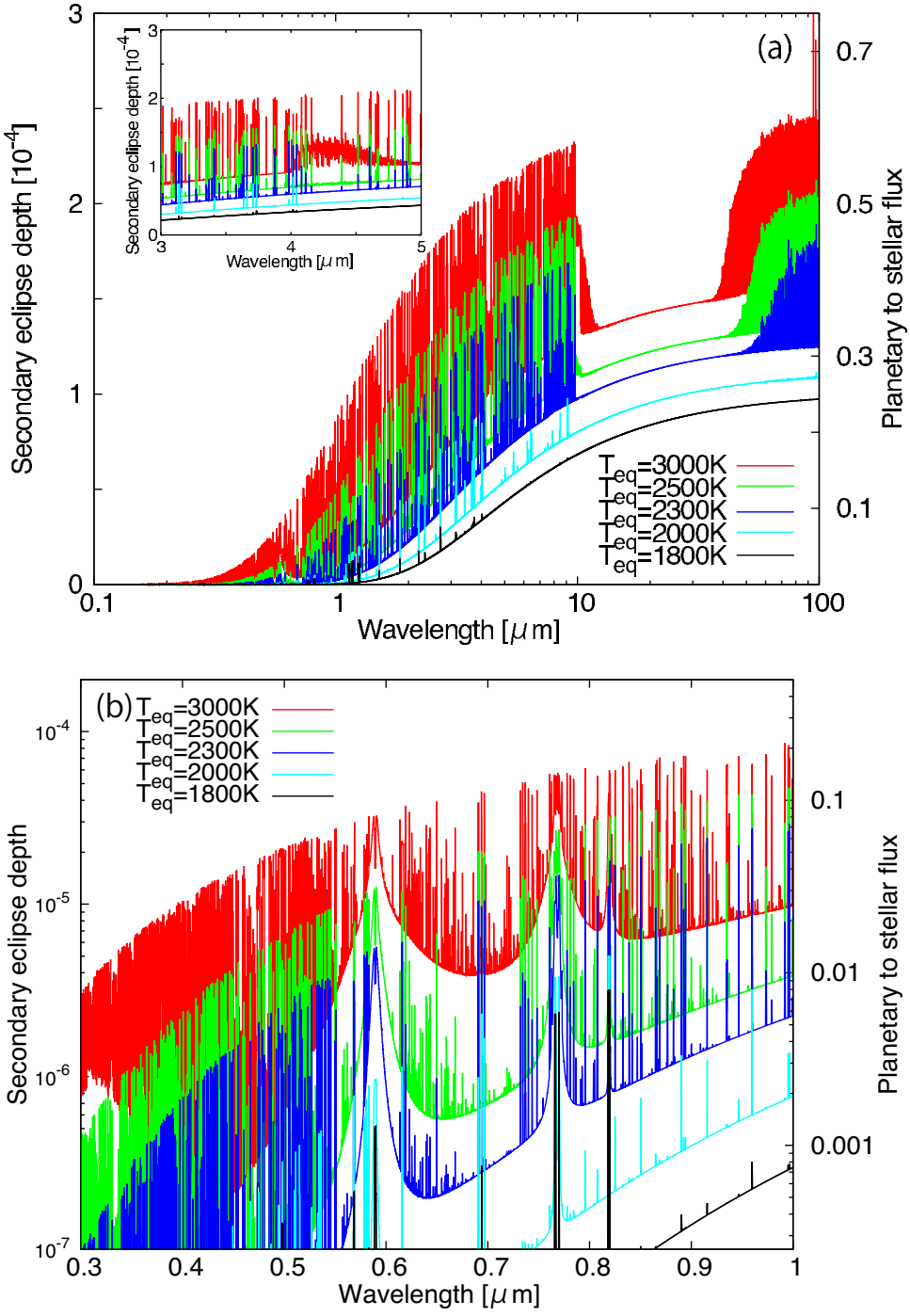

Figure 2.6: Predicted dayside-averaged emission spectra of a hot rocky super-Earth of 2 $R_\oplus$ in secondary eclipse that has a mineral atmosphere in equilibrium with an underlying BSE magma ocean. The secondary eclipse depth (see eq. [2.17]) is shown as a function of wavelength in the range of (a) 0.1–100 μm and (b) 0.3–1 μm. The inset in the Fig.(a) is an enlarged view of the spectra in 3–5 μm. Five equilibrium temperatures are chosen: $T_{\rm eq}$ = 1800 K (black), 2000 K (cyan), 2300 K (blue), 2500 K (green), and 3000 K (red). The corresponding atmospheric structures are shown by dashed lines in Fig. 2.4. The host star is assumed to be a Sun-like star with radius of 1 $R_\odot$ (i.e., the planetary/stellar radius ratio being 0.02) and emit the blackbody radiation of 6000 K.

2.4.2 Detectability

We evaluate the detectability of the mineral atmosphere of an HRSE for near-future space-based secondary-eclipse observation. The photometric accuracy of the transit/eclipse observation from space depends on the instrument measurement noise, the intrinsic stellar variability, and the shot noise from photon statistics (e.g. Clanton et al. 2012). In this section, we quantify the photometric accuracy required for the line detection and discuss the feasibility, assuming the ideal case that the total noise is dominated by the shot noise (i.e. the photon-noise limit). To quantify the detectability for the photon-noise limit, we introduce the signal-to-noise ratio of the detection of the secondary eclipse as

$$(S/N)_{\Delta\lambda} = \frac{N_p}{\sqrt{N_*}}, \tag{2.19}$$

$$\simeq \epsilon_{\lambda,\Delta\lambda}\sqrt{\frac{At_{\rm obs}}{\mathfrak{R}}\frac{R_*^2}{d^2}\frac{\pi B_{\Delta\lambda}(T_*)}{h}}, \tag{2.20}$$

where $\Delta\lambda$ is the band width used for the detection of the secondary eclipse, N_* is the photon counts of the star, A is the photon collecting area, $t_{\rm obs}$ is the exposure time, d is the distance of the system, $\mathfrak{R}$ is the resolving power of the spectra, $\epsilon_{\lambda,\Delta\lambda}$ is the depth of the secondary eclipse within $\Delta\lambda$, N_p is the photon count of the planet, $B_{\Delta\lambda}(T_*)$ is the blackbody radiation integrated over a wavelength band (i.e., $\int_{\Delta\lambda} B_\lambda(T_*)d\lambda/\Delta\lambda$), and h is the Planck constant.

Figure 2.7 plots the theoretical (solid line), mock (cross), and blackbody (dotted lines) secondary-eclipse-depth spectra for $T_{\rm eq} = 3000$ K (a), 2500 K (b), and 2300 K (c). When calculating the mock spectra, we use the false normal random number generation circuit (William et al. 1996), and include the statistical noise, assuming the normal distribution with the standard deviation $\sigma = \sqrt{N_*}$. We assume $A = (5/2\,{\rm m})^2$ as a fiducial value, roughly corresponding to that of James Webb Space Telescope (JWST; Clampin 2008), and that $\mathfrak{R} = 100$ in 0.3-1 μm and 10 in 1-100 μm, $t_{\rm obs} = 10$ hours, and $d = 100$ pc. The blackbody spectra are calculated from equation (2.17) with the assumption $F_{p,\lambda} = B_\lambda(T)$.

As demonstrated in Fig. 2.7, the spectral features of Na, K and SiO are represented by the blackbody spectra with different temperatures (i.e., brightness temperature $T_{\rm br}$). For example, in the case of $T_{\rm eq} = 3000$ K (see Fig. 2.7a), $T_{\rm br} \simeq 3200$ K at 10μm, and 2700 K at 4μm due to SiO. Additionally, although not shown, $T_{\rm br} \simeq 3500$ K at 0.6 μm and at 0.8μm (which are due to Na and K, respectively), and 3100 K at 100 μm (SiO). At the other wavelengths, $T_{\rm br} \simeq T_{\rm g}$ (e.g., $T_{\rm br} = 2350$ K for $T_{\rm eq} = 3000$ K), because the atmosphere is optically thin at those wavelengths.

Comparing the mock spectra with the blackbody spectra, one can quantify the detectability of the spectral features of Na, K and SiO. The error bars become larger in both shorter and

longer wavelength regions, because the number of incident photons (i.e., $B_{\Delta\lambda}(T_*)$) is small in such wavelength regions. Also, the values of $\mathfrak{R}$, which are assumed to be 100 in 0.1-1 μm and 10 in 1-100 μm, affect the value of $(S/N)_{\Delta\lambda}$. As shown in Figure 2.7a, the spectral features of SiO are sufficiently detectable at 4, 10 and 100 μm for $T_{\rm eq}$ = 3000 K. The SiO feature is also sufficiently detectable at 10 μm for $T_{\rm eq}$ = 2500 K (Fig. 2.7b), while the feature is marginally undetectable for $T_{\rm eq}$ = 2300 K (Fig. 2.7c).

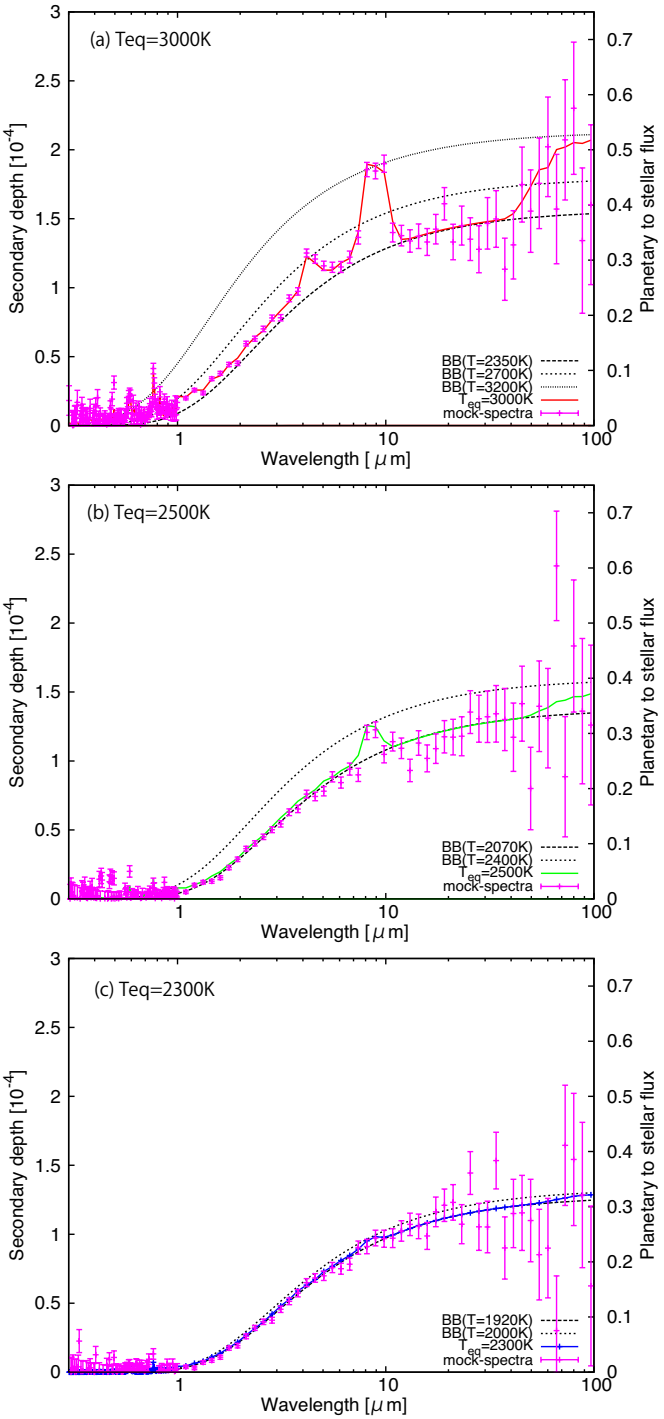

Figure 2.7: The secondary eclipse depths theoretically predicted and the mock observational spectrum compared to the blackbody spectra (BB). The secondary eclipse depths are shown as functions of wavelength for $T_{\rm eq}$ = (a) 3000 K, (b) 2500 K, and (c) 2300 K. The black dotted lines show the secondary eclipse depths of the blackbody, temperatures of which are indicated by "BB(T)". The bars show the mock spectrum calculated based on the photon-noise limit with the assumptions that $R_* = 1\ R_\odot$, $R_p = 0.02 R_\odot$, $A = \pi(5{\rm m}/2)^2$, $t_{\rm obs} = 10$ hours, $\mathfrak{R} = 100$ in 0.3-1 μm and 10 in 1-100 μm, and $d = 100$ pc (see the text for the details). The corresponding atmospheric structures are shown by dashed lines in Fig. 2.4.

The signal-to-noise ratio for detecting the line absorption spectral feature of the secondary eclipse depth is generally smaller than that for the secondary eclipse detection. Thus, we define the secondary eclipse depth relative to that with no atmospheric feature (i.e., blackbody with $T_{\rm g}$), $\eta_{\lambda,\Delta\lambda}$ as

$$\eta_{\lambda,\Delta\lambda} \equiv \left| \int_{\lambda}^{\lambda+\Delta\lambda} \frac{\epsilon_\lambda - \epsilon_{{\rm BB},\lambda}(T_{\rm g})}{\epsilon_\lambda} \frac{d\lambda}{\Delta\lambda} \right|, \tag{2.21}$$

where $\epsilon_{{\rm BB},\lambda}(T_{\rm g})$ is the secondary eclipse depth by the blackbody radiation with $T_{\rm g}$. Using $\eta_{\lambda,\Delta\lambda}$, we estimate the detectability of the line spectral features. From equations (2.20) and (2.21), we introduce a new quality, $(S/N)_{L,\Delta\lambda}$, that is defined as

$$(S/N)_{L,\Delta\lambda} = \eta_{\lambda,\Delta\lambda}(S/N)_{\Delta\lambda}. \tag{2.22}$$

When $(S/N)_{L,\Delta\lambda}$ is sufficiently large, we can detect the line spectral feature of the secondary eclipse depth. Thus, if the minimum value of $(S/N)_{L,\Delta\lambda}$ required to detect a line spectral feature, $|(S/N)_{L,\Delta\lambda}|_{\rm min}$, is 3, $(S/N)_{\Delta\lambda} \geq 3/\eta_{\lambda,\Delta\lambda}$ is required to do so.

Figure 2.8a shows $\eta_{\lambda,\Delta\lambda}$ for $T_{\rm eq}$ = 3000 K (red), 2500 K (green), and 2300 K (blue) with $\mathfrak{R}$ = 100 in 0.3-1 μm and 10 in 1-100 μm. As shown in Figure 2.8a, $\eta_{\lambda,\Delta\lambda}$ takes large values at some wavelengths, because of the strong line features: $\eta_{\lambda,\Delta\lambda} \sim 1$ at 0.6 μm (Na) and ~ 0.35 at 10 μm (SiO) for $T_{\rm eq}$ = 3000 K (red). $\eta_{\lambda,\Delta\lambda}$ is large at ~ 4 μm because of the SiO feature peak only for $T_{\rm eq}$ = 3000 K (red), since the SiO feature is weaker than Na and K features for $T_{\rm eq}$ = 2300 K and 2500 K. Also, Figure 2.8b shows $|(S/N)_{L,\Delta\lambda}|_{\rm min}/\eta_{\lambda,\Delta\lambda} (\equiv |(S/N)_{\Delta\lambda}|_{\rm min})$ for $T_{\rm eq}$ = 3000 K (red), 2500 K (green), and 2300 K (blue), assuming $|(S/N)_{L,\Delta\lambda}|_{\rm min} = 3$ as a minimum fiducial value to detect the line spectral feature with $\mathfrak{R}$ = 100 in 0.3-1 μm and 10 in 1-100 μm. We obtain that $|(S/N)_{\Delta\lambda}|_{\rm min} \lesssim 100$ around 4, 10 and 100 μm; for example, $|(S/N)_{\Delta\lambda}|_{\rm min} \simeq 60$ at 10 μm for $T_{\rm eq}$ = 2300 K (blue) and $|(S/N)_{\Delta\lambda}|_{\rm min} \simeq 10$ at 4 μm for $T_{\rm eq}$ = 3000 K (red). Thus, observation of an HRSE in secondary eclipse can detect the components of the mineral atmosphere such as Na, K and SiO, provided its signal to noise ratio is larger than $|(S/N)_{\Delta\lambda}|_{\rm min}$.

Finally, we estimate the limiting distance $d_{\rm max}$ interior to which an HRSE with the mineral atmosphere is detectable with a given $|(S/N)_{\Delta\lambda}|_{\rm min}$, for the photon-noise limiting case. From equation (2.20), $d_{\rm max}$ is written as

$$d_{\rm max}\left\{|(S/N)_{\Delta\lambda}|_{\rm min}\right\} = \frac{\epsilon_{\lambda,\Delta\lambda}}{|(S/N)_{\Delta\lambda}|_{\rm min}} \times \sqrt{\frac{A t_{\rm obs}}{\mathfrak{R}} \frac{\pi B_{\Delta\lambda}(T_*)}{h}} R_*. \tag{2.23}$$

Figure 2.9 shows $d_{\max}$ as a function of wavelength for $|(S/N)_{\Delta\lambda}|_{\min} = 3/\eta_{\lambda,\Delta\lambda}$ (i.e., the minimum signal-to-noise ratio for the detection of line spectral features within secondary eclipse depth; shown by solid lines) or 3 (i.e., the minimum signal-to-noise ratio for the detection of the secondary eclipse depth itself; shown by dotted lines); $R_* = 1\ R_\odot$, $R_p = 0.02 R_\odot$, $A = \pi(5\mathrm{m}/2)^2$, $t_{\rm obs} = 10$ hours, and $\mathfrak{R} = 10$ in 1-100 μm and 100 in 0.3-1 μm. In particular, the solid lines show the limiting distance $d_{\max}$ to detect the SiO line spectral features around 4, 10, and 100 μm. Note that $d_{\max}$ around 4 μm is not shown for $T_{\rm eq} = 2300$ K and 2500 K, because the Na, K and SiO features in those cases are indistinguishable from each other when integrating the secondary eclipse depth with respect to wavelength with $\mathfrak{R} = 10$.

Table 2.2 summarizes $d_{\max}$ for the SiO detection. The limiting distance $d_{\max}$ increases with increasing $T_{\rm eq}$, because an HRSE with higher $T_{\rm eq}$ shows greater planetary emission and more remarkable line absorption spectral feature of the secondary eclipse depths. Thus, the mineral atmospheres of more distant HRSEs would be also detectable if they have higher $T_{\rm eq}$.

Table 2.2: Limiting distance for detection of the SiO line features

$d_{\max}$	$T_{\rm eq} = 2300$ K	$T_{\rm eq} = 2500$ K	$T_{\rm eq} = 3000$ K
4μm	-	-	340pc
10μm	30pc	150pc	430pc
100μm	3.5pc	8.7pc	40pc

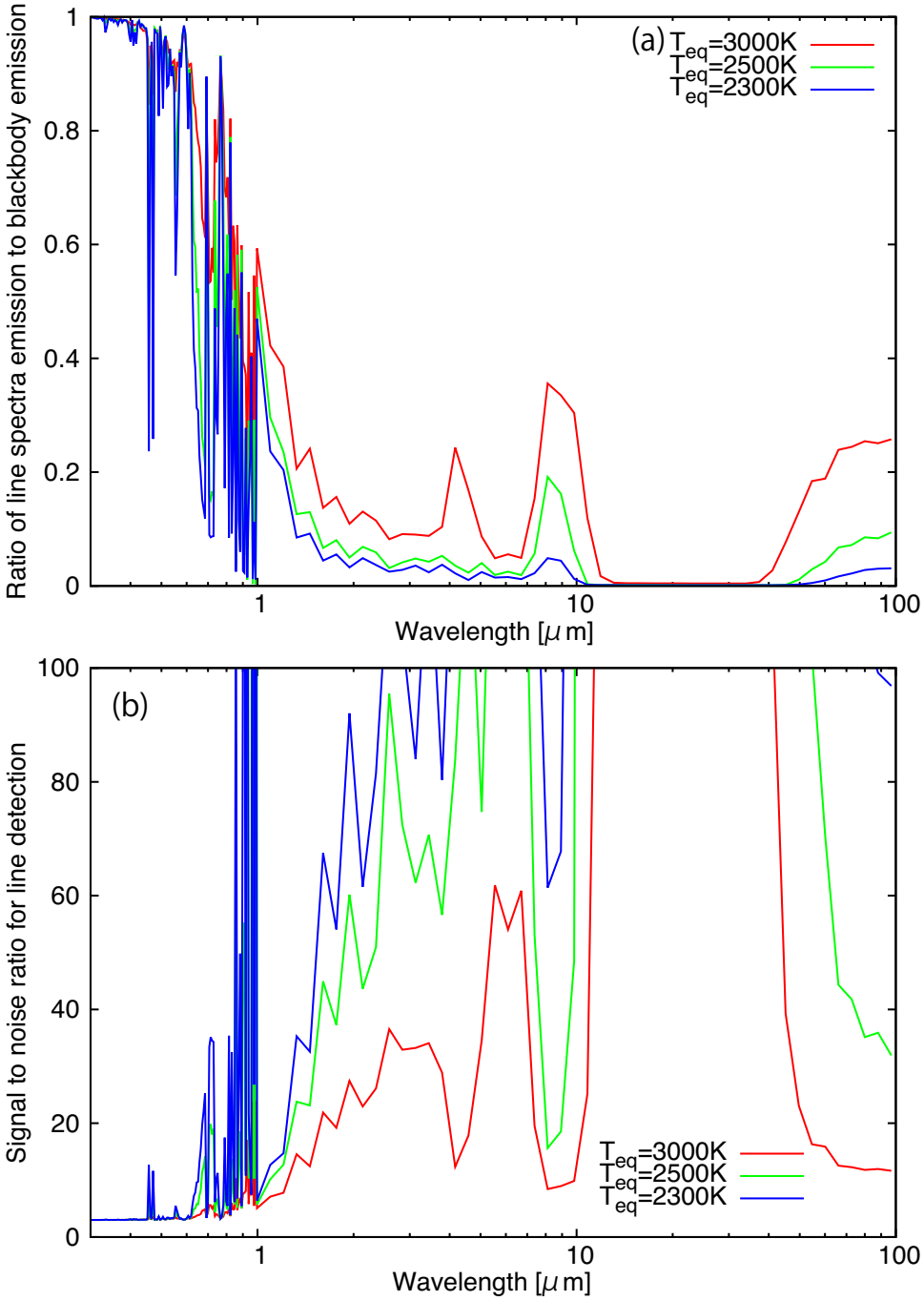

Figure 2.8: (a) The secondary eclipse depth relative to that of blackbody with $T_{\rm g}$ ($\eta_{\lambda,\Delta\lambda}$; see eq. [2.21]) and (b) the minimum signal-to-noise ratio required to distinguish the emission spectral features from the blackbody emission with $T_{\rm g}$ ($|(S/N)_{\Delta\lambda}|_{\rm min}$; see eq. [2.22]). $\Re = 100$ in 0.3-1 μm and 10 in 1-100 μm. Three equilibrium temperatures are chosen: $T_{\rm eq} = 3000$ K (red), 2500 K (green), 2300 K (blue). The corresponding atmospheric structures are shown by dashed lines in Fig. 2.4. The host star is assumed to be a Sun-like star with radius of 1 $R_\odot$ (i.e., the planetary/stellar radius ratio being 0.02) and emit the blackbody radiation of 6000 K.

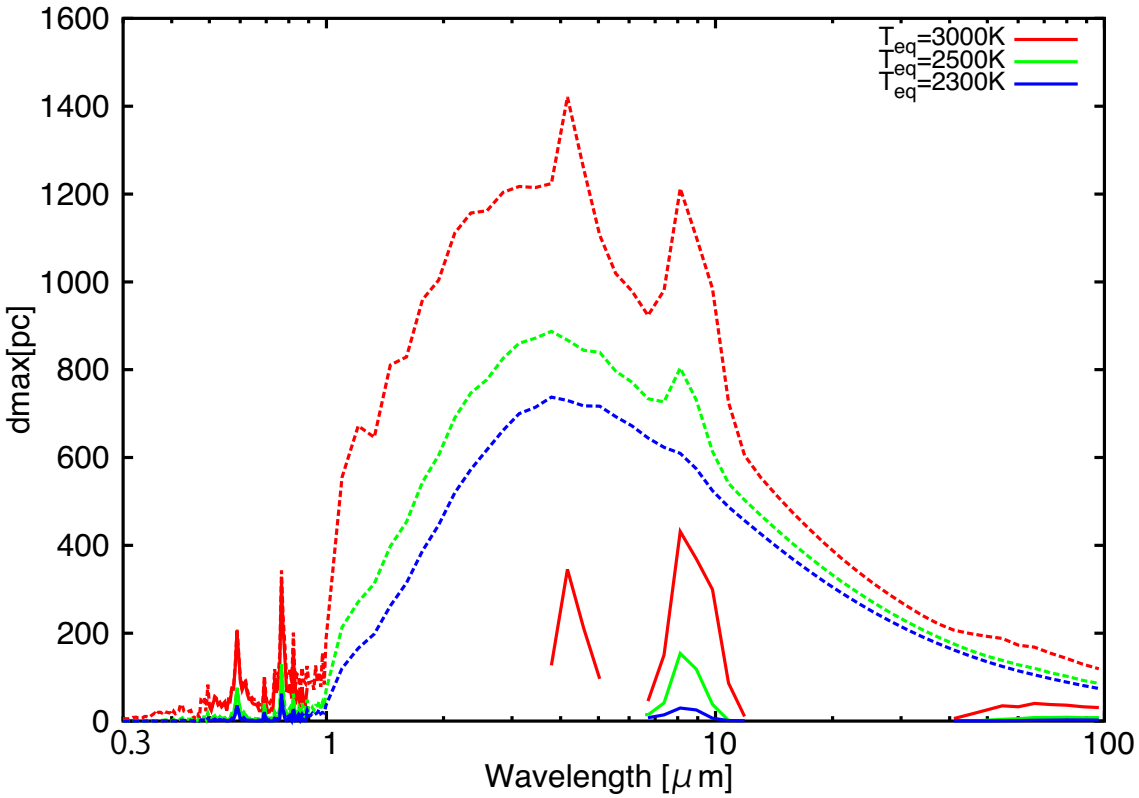

Figure 2.9: The limiting distance $d_{\rm max}$ (see eq. [2.23] for the definition), interior to which an HRSE with the model atmosphere orbiting a Sun-like star is detectable with $(S/N)_{\Delta\lambda}$ by a given instrument, is shown as a function of wavelength for three equilibrium temperatures $T_{\rm eq}$ = 3000 K (red), 2500 K (green), and 2300 K (blue) with the assumption that $R_* = 1\ R_\odot$, $R_p = 0.02 R_\odot$, $A = \pi(5{\rm m}/2)^2$, $t_{\rm obs}$ = 10 hours, and $\Re$ = 10 in 1-100 μm and 100 in 0.3-1 μm. The corresponding atmospheric structure is shown in Fig. 2.4. The solid lines show the limiting distance $d_{\rm max}$ to detect the line spectral features within secondary eclipse depth around 4, 10, and 100 μm, assuming $(S/N)_{\Delta\lambda} = 3/\eta$ shown in Figure 2.8b. The dotted lines show the limiting distance $d_{\rm max}$ to detect the secondary eclipse depth itself, assuming $(S/N)_{\Delta\lambda}$=3. The host star is assumed to be a Sun-like star with radius of 1 $R_\odot$ (i.e., the planetary/stellar radius ratio being 0.02) and emit the blackbody radiation of 6000 K.

2.4.3 Application to known HRSEs

We show the simulated secondary-eclipse-depth spectra of four known close-in super-Earths, CoRoT-7b, Kepler-10b, Kepler-78b, and 55 Cnc e in Fig. 2.10. Within the 1σ errors of their observed masses and radii, it is possible that those super-Earths are naked rocky planets. Note that, according to Dragomir et al. (2014), the 1σ upper limit on the measured 55 Cnc e's density just reaches the pure rock regime. If so, they have mineral atmospheres, because of high $T_{\rm eq}$ (see Table 2.3). In the simulations, we have assumed $\mathfrak{R} = 10$ in 1-100 μm and 100 in 0.3-1 μm. The values of the planetary and stellar parameters that we have used are listed in Table 2.3.

The secondary eclipse depth becomes large, as R_p/R_* increases and $T_{\rm eq}$ increases. Thus, the secondary eclipse depth of 55 Cnc e ($R_p/R_* = 2.12\ R_\oplus/R_\odot$) is largest, while that of Kepler-10b ($R_p/R_* = 1.39\ R_\oplus/R_\odot$) is smallest. Despite of its larger R_p/R_*, the secondary eclipse depth of CoRoT-7b is smaller than that of Kepler-78b, because $T_{\rm eq}$ of CoRoT-7b is smaller than that of Kepler-78b.

Prominent absorption features are found around $\lambda = 0.6$ μm (Na), 0.77 μm (K), 4 μm, 10 μm and 100 μm (SiO). In particular, in the cases of Kepler-10b and 55 Cnc e, those features would be detectable by the near-future space-based observation that we have assumed in subsection 2.4.2, because the distances of these systems are shorter than $(R_*/R_\odot)^{-1}\ (R_p/2R_\oplus)^2\ d_{\rm max}$ from equations (2.17) and (2.23).

Table 2.3: Assumed planetary and stellar parameters

	Corot-7b[3]	Kepler-10b[4]	Kepler-78b[5]	55 Cnc e[6]
M_p	7.42 $M_\oplus$	3.33 $M_\oplus$	1.69 $M_\oplus$	8.09 $M_\oplus$
R_p	1.58 $R_\oplus$	1.47 $R_\oplus$	1.20 $R_\oplus$	1.99 $R_\oplus$
D	0.0172AU	0.0168 AU	0.0092 AU	0.0155 AU
$T_{\rm eq}$	2550 K	3090 K	3000 K	2700 K
R_*	0.82 $R_\odot$	1.06 $R_\odot$	0.74 $R_\odot$	0.94 $R_\odot$
T_*	5250 K	5700 K	5200 K	5200 K
distance	150pc	173pc	-	12.3pc

Notes. [3]Hatzes et al. (2011), Bruntt et al. (2010), Léger et al. (2009), [4]Dumusque et al. (2014), Fressin et al. (2011), [5]Howard et al. (2013), [6]Dragomir et al. (2014), Nelson et al. (2014), Ehrenreich et al. (2012)

Demory et al. (2012) have already reported the detection of the secondary eclipse depth of 55 Cnc e with Spitzer Space Telescope at 4.5 μm. The measured brightness temperature of 2360 $\pm$ 300 K is consistent with our result shown in Fig. 2.10(d), although the error is large. Also, the SiO IR-absorption features of an HRSE that is brighter and closer than 55 Cnc e would be

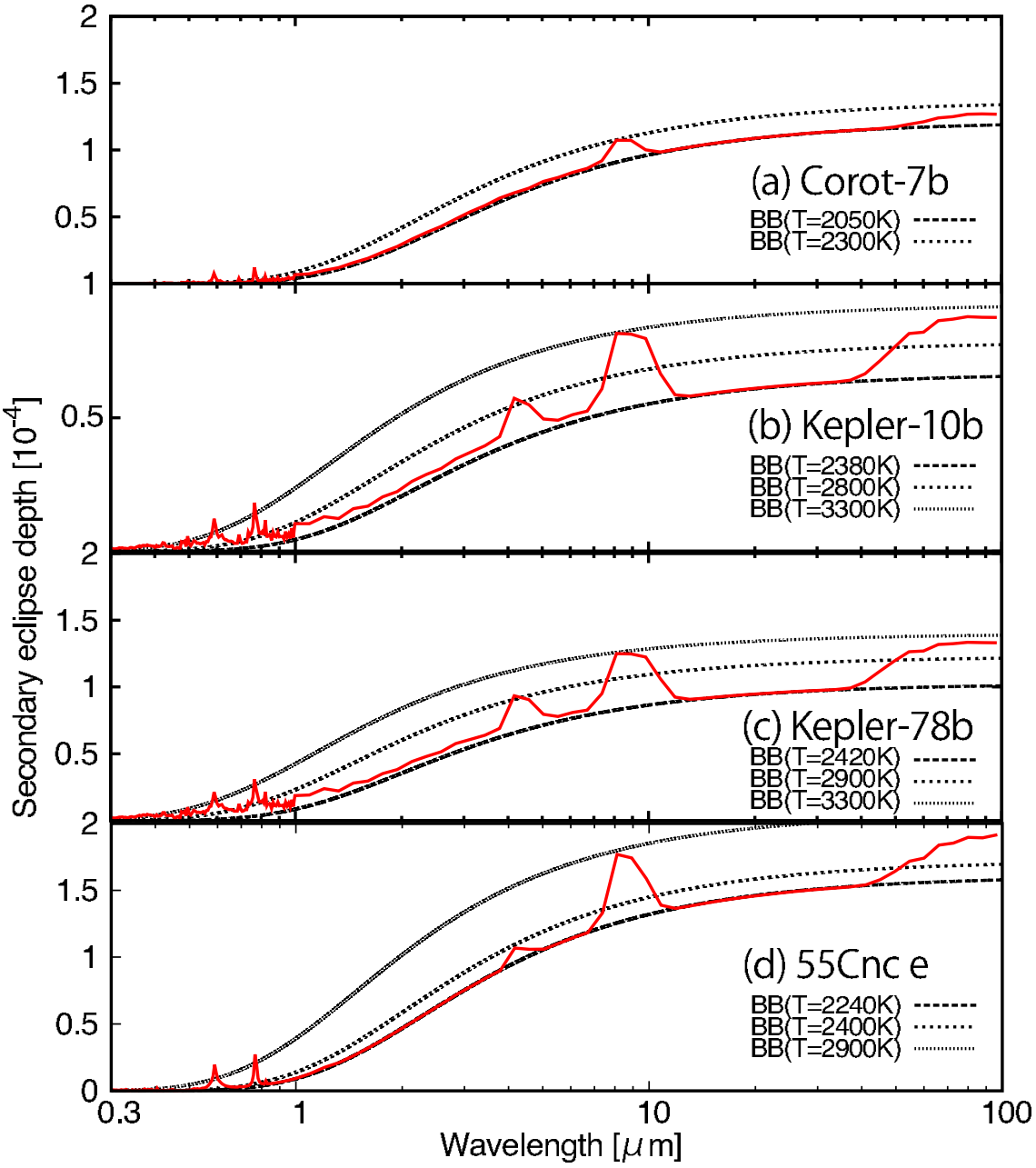

Figure 2.10: The secondary eclipse depths theoretically predicted for (a) Corot-7 b, (b) Kepler-10 b, (c) Kepler-78 b and (d) 55 Cnc e, shown as a function of wavelength, assuming that they have the mineral atmosphere. The solid lines show the predicted secondary eclipse depth. The black dotted lines show the secondary eclipse depths of the blackbody, temperatures of which are indicated by "BB(T)". We have assumed $\mathfrak{R} = 100$ in 0.3-1 μm and 10 in 1-100 μm and the planets' parameters shown in Table 2.3.

detectable with Spitzer in the IRAC 4.5 and 8 μm channel.

Using equations (2.20) and (2.21), we define the line contrast to the total flux, $C_{L,(\lambda,\Delta\lambda)}$ as

$$C_{L,(\lambda,\Delta\lambda)} \equiv \eta_{\lambda,\Delta\lambda}\, \epsilon_{\lambda,\Delta\lambda}. \tag{2.24}$$

The photometric accuracy should be smaller than $C_{L,(\lambda,\Delta\lambda)}$ in order to detect the line spectra feature of the secondary eclipse depth. There are several proposed missions that aim to characterize transiting exoplanets, such as Fast Infrared Exoplanet Spectroscopy Survey Explorer (FINESSE; e.g. Deroo et al. 2012) and the Exoplanet Characterization Observatory (EChO; e.g. Tinetti et al. 2012). Here we compare our results with the accuracy of EChO. Figure 2.11 shows the theoretical (solid line) and mock-EChO (bars) secondary-eclipse-depth spectra for a super-Earth with a mineral atmosphere, using 55 Cnc e's parameters. Then, we create the mock-EChO spectra with $\Re$ of 50 in 1–5 μm and 30 in 5–16 μm, and the photometric accuracy of EChO in Chemical census mode (Waldmann & Pascale 2014) [7]. Our result demonstrates that EChO has enough accuracy to detect the SiO feature of the mineral atmosphere of 55 Cnc e around 4 μm and 10 μm.

Table 2.4 shows the line contrasts C_L of Na (0.59 μm), K (0.77 μm) and SiO (4 μm, 10 μm and 100 μm) for $T_{\rm eq}$ = 2300 K, 2500 K, and 3000 K ($\Re$ = 100 for $\lambda \leq 1$ μm and $\Re$ = 10 for $\lambda \geq 1$ μm), and 55 Cnc e's parameters ($\Re$ = 100 for $\lambda \leq 1$ μm, $\Re$ = 50 for 1 μm $\leq \lambda \leq 5$ μm and $\Re$ = 30 for $\lambda \geq 5$ μm). The photometric accuracy of EChO in Chemical Census mode of 55 Cnc e (Waldmann & Pascale 2014) is also shown in Table 2.4. Note that the values of C_L at 4 μm are not shown for $T_{\rm eq}$ = 2300 K and 2500 K, because the Na, K and SiO features in those cases are indistinguishable with $\Re$ = 10. We obtain that $C_{L,(\lambda,\Delta\lambda)} \gtrsim 10$ ppm for Na (0.59 μm), K (0.77 μm) and SiO (4 μm, 10 μm and 100 μm); for example, $C_{L,(\lambda,\Delta\lambda)} \sim 14$ ppm at 0.77 μm and 24 ppm at 10 μm for $T_{\rm eq}$ = 2500 K and $C_{L,(\lambda,\Delta\lambda)} \sim 26$ ppm at 0.59 μm, 34 ppm at 0.77 μm, and 67 ppm at 10 μm for $T_{\rm eq}$ = 3000 K. The required photometric accuracy to detect the SiO features at 4 and 10 μm is achievable with the Chemical Census mode of EChO for 55 Cnc e.

Table 2.4: Values of the line contrast

the line contrast $C_{L,(\lambda,\Delta\lambda)}$	$T_{\rm eq}$ = 2300 K	$T_{\rm eq}$ = 2500 K	$T_{\rm eq}$ = 3000 K	55 Cnc e	Accuracy of EChO
Na at 0.59 μm	4.4ppm	9.3ppm	26ppm	19ppm ($\Re$ = 100)	-
K at 0.77 μm	6.4ppm	14ppm	36ppm	26ppm ($\Re$ = 100)	-
SiO at 4 μm	-	-	30ppm	16ppm ($\Re$ = 50)	12ppm ($\Re$ = 50)
SiO at 10 μm	4.6ppm	24ppm	67ppm	54ppm ($\Re$ = 30)	24ppm ($\Re$ = 30)
SiO at 100 μm	4.0ppm	13ppm	50ppm	36ppm ($\Re$ = 30)	-

[7] Waldmann & Pascale (2014) showed the simulated EChO observation of 55 Cnc e assuming a CO_2 and H_2O atmosphere model. We use the noise level assumed in their Figure 9 because the depth of their spectra is similar to ours.

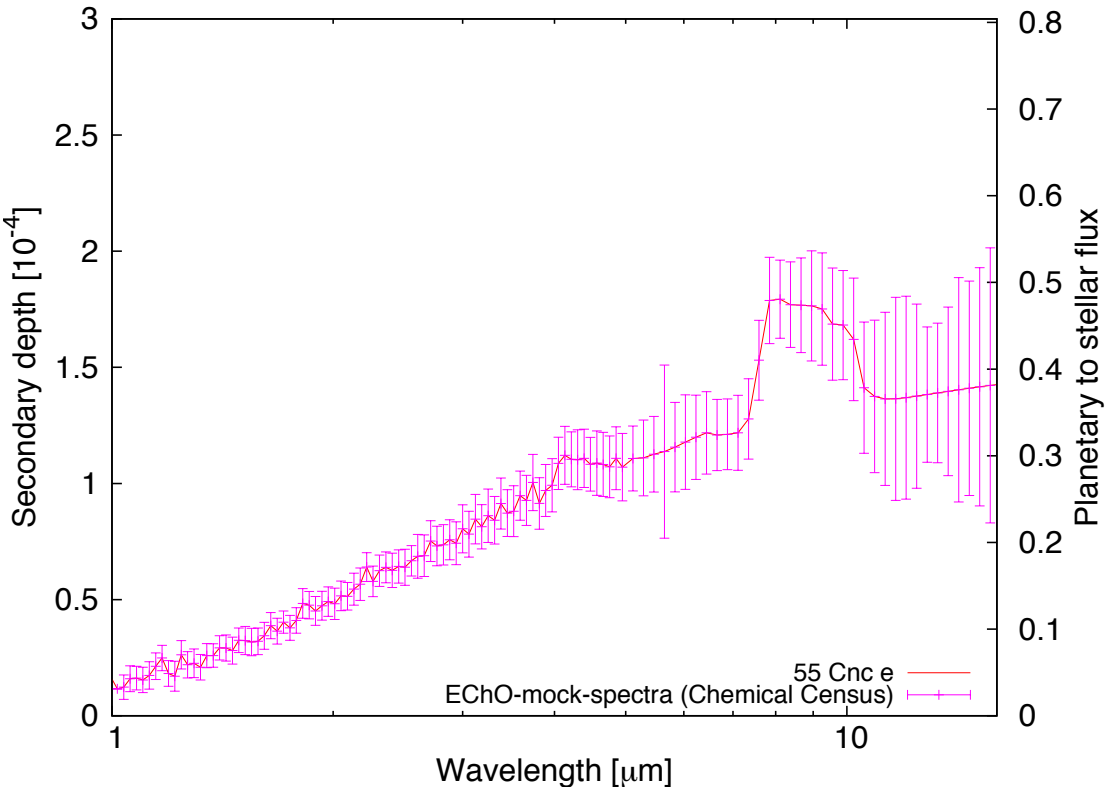

Figure 2.11: The secondary eclipse depths theoretically predicted and the mock-EChO observational spectrum for 55 Cnc e with the mineral atmosphere. The secondary eclipse depth is shown as a function of wavelength. The solid line shows the predicted secondary eclipse depth. The magenta bars show the mock-EChO observational spectrum (Waldmann & Pascale 2014). We have assumed $\mathfrak{R} = 50$ in 1-5 μm and 30 in 5-16 μm and 55 Cnc e's parameters: $M_p = 8.09$ $M_\oplus$, $R_p = 1.99$ $R_\oplus$, $a = 0.0155$AU, $T_{\rm eq} = 2700$ K R_*=0.94 $R_\odot$ and T_*=5200K.

2.4.4 How many HRSEs are detectable via near-future observation?

The *Kepler* space telescope discovered 4250 planet candidates (http://exoplanets.org, as of 30 Nov. 2014). The Kepler Objects of Interest (KOIs) include super-Earth-size objects with short periods (i.e., HRSEs), in particular, 751 objects with $R_p \leq 2R_\oplus$ orbiting stars with $T_{\rm eff} = 5300$-6000 K. Among them, there are 60 KOIs with $T_{\rm eq} > 2300$ K. If they are naked rocky planets, their mineral atmospheres can be identified by secondary-eclipse observations with sufficient signal-to-noise ratios. We estimate the expected number of such HRSEs detectable by near future observations.

Assuming a uniform distribution of G-type stars, the number of the detectable HRSEs, $\overline{N_{\rm HRSE}}$, is given by

$$\overline{N_{\rm HRSE}} \approx r N_{\rm G} \frac{4\pi}{3} \left[d_{\rm max} \left\{ (S/N)_{\Delta\lambda} \right\} \right]^3 , \tag{2.25}$$

where r is the occurrence rate of HRSEs with $T_{\rm eq} \geq 2300$ K hosted by G-type stars and $N_{\rm G}$ is the number density of G-type stars. The HRSEs with $T_{\rm eq} \geq 2300$ K, which should exhibit the prominent emission features (Fig. 2.7), correspond to planets with period $P \lesssim 2$ days around G-type stars. Fressin et al. (2013) estimated, using KOI host stars, the occurrence rate of planets with $1.25R_\oplus < R_p < 2R_\oplus$ hosted by G-type stars to be close to 0.35. They also estimated the occurrence rate of planets with $1.25R_\oplus < R_p < 2R_\oplus$ and $0.8 < P < 2$ days to be $1.7(\pm 0.3) \times 10^{-3}$. Using their results, the occurrence rate of the planets with $1.25R_\oplus < R_p < 2R_\oplus$ and $0.8 < P < 2$ days hosted by G-type stars is estimated to be $r \sim 6 \times 10^{-4}$. Here we use $r = 6 \times 10^{-4}$ as a fiducial value of the occurrence rate.

In section 2.4.2, we estimated $d_{\rm max} \left\{ (S/N)_{\Delta\lambda} = 3/\eta_{\lambda,\Delta\lambda} \right\}$ to be 430 pc ($T_{\rm eq} = 3000$ K), 150 pc ($T_{\rm eq} = 2500$ K) and 30 pc ($T_{\rm eq} = 2300$ K) for 10 μm observation (see Fig. 2.9 and Table 2.2). These HRSEs with $T_{\rm eq} = 2300$ K, 2500 K and 3000 K have the orbital period $P \sim 0.93$, 1.6 and 2.0 days, respectively. Hence we take the simple mean $\left[(430^3 + 150^3 + 30^3)/3 \right]^{1/3}$ pc ~ 300 pc as a fiducial value of the limiting distance for HRSEs with $0.8 < P < 2$ days. Inputting $r = 6 \times 10^{-4}$ % and $N_{\rm G} \sim 6 \times 10^{-3} {\rm pc}^{-3}$ (see a recent review by Traub & Oppenheimer 2011) in equation (2.25), we find that within 300 pc there are approximately 400 HRSEs whose 10 μm SiO features are detectable . Taking the transiting probability of ~ 0.2 ($\sim R_\odot/D$ for $P = 1.3$ days) into account, one will be able to detect the 10 μm SiO features from ~ 80 transiting HRSEs by a 5 m space telescope equipped with a photon-noise limited instrument.

Chapter 3

Hydrodynamic Models

本章については、5年以内に雑誌等で刊行予定のため、非公開。

Chapter 4

Results

本章については、5年以内に雑誌等で刊行予定のため、非公開。

Chapter 5

Discussion

本章については、5年以内に雑誌等で刊行予定のため、非公開。

Chapter 6

Conclusions and Summary

本章については、5年以内に雑誌等で刊行予定のため、非公開。

Acknowledgment

I would like to show my greatest appreciation to Associate Professor M. Ikoma whose comments and suggestions were innumerably valuable throughout the course of my study. His comments, suggestion and discussion have guided this study properly. Without his guidance, the completion of this thesis would not be possible.

I really appreciate Professor K. Seki, Professor Y. Suto, Professor T. Imamura of the University of Tokyo and Associate Professor N. Terada of Tohoku University whose constructive comments have helped improved this thesis greatly. Special thanks also go to Professor E. Tajika and Professor S. Sugita of the University of Tokyo whose comments made enormous contributions to my work. Thanks are offered to Fellow H. Nagahara of the Earth-Life Science Institute and Professor T. Nakamoto of Tokyo Institute of Technology for help in my previous study. I owe an important debt to Associate Professor Y. Abe who gave me invaluable comments and warm encouragements. I also owe a very important debt to Associate Professor K. Kasahara and Assistant Professor H. Kawahara whose opinions and information have helped me very much throughout the production of this study. I would like to thank Dr. A. García Muñoz of Technical University of Berlin whose comments and documents have helped me very much throughout the construction of my own hydrodynamic code. I would also like to thank for useful advice and fruitful discussion offered by the other members in Ikoma-lab seminar, Wakusei-seminar and System-seminar.

References

Adams, E. R., Seager, S., & Elkins-Tanton, L. 2008, ApJ, 673, 1160

Aldrovandi, S. M. V., & Pequignot, D. 1973, A&A, 25, 137

Allard, F., Hauschildt, P. H., & Schwenke, D. 2000, ApJ, 540, 1005

Allende Prieto, C., Lambert, D. L., Hubeny, I., & Lanz, T. 2003, ApJS, 147, 363

Asimov, P. D., & Ghiorso, M. S. 1998, American Mineralogist, 83, 1127

Badnell, N. R. 2006, ApJS, 167, 334

Banks, P. M., & Kockarts, G. 1973, Aeronomy.

Barnes, R., Raymond, S. N., Greenberg, R., Jackson, B., & Kaib, N. A. 2010, ApJL, 709, L95

Barton, E. J., Yurchenko, S. N., & Tennyson, J. 2013, MNRAS, 434, 1469

Bean, J. L., Miller-Ricci Kempton, E., & Homeier, D. 2010, Nature, 468, 669

Bochinski, J. J., Haswell, C. A., Marsh, T. R., Dhillon, V. S., & Littlefair, S. P. 2015, ApJL, 800, L21

Brogi, M., Keller, C. U., de Juan Ovelar, M., Kenworthy, M. A., de Kok, R. J., Min, M., & Snellen, I. A. G. 2012, A&A, 545, L5

Bruntt, H., et al. 2010, A&A, 519, A51

Budaj, J. 2013, A&A, 557, A72

Burgers, J. M. 1969, Flow Equations for Composite Gases

Butler, K., & Zeippen, C. J. 1994, A&AS, 108, 1

Chamberlain, J. W., & Hunten, D. M. 1987, Theory of planetary atmospheres. An introduction to their physics andchemistry.

Chambers, J. E. 2009, Annual Review of Earth and Planetary Sciences, 37, 321

Charbonneau, D., et al. 2005, ApJ, 626, 523

Charbonneau, D., et al. 2009, Nature, 462, 891

Charbonneau, D., Brown, T. M., Latham, D. W., & Mayor, M. 2000, ApJL, 529, L45

Charbonneau, D., Brown, T. M., Noyes, R. W., & Gilliland, R. L. 2002, ApJ, 568, 377

Chatzikos, M., Ferland, G. J., Williams, R. J. R., Porter, R., & van Hoof, P. A. M. 2013, ApJ, 779, 122

Cincunegui, C., & Mauas, P. J. D. 2001, ApJ, 552, 877

Claire, M. W., Sheets, J., Cohen, M., Ribas, I., Meadows, V. S., & Catling, D. C. 2012, ApJ, 757, 95

Clampin, M. 2008, in Society of Photo-Optical Instrumentation Engineers (SPIE) Conference Series, Vol. 7010, Society of Photo-Optical Instrumentation Engineers (SPIE) Conference Series

Clanton, C., Beichman, C., Vasisht, G., Smith, R., & Gaudi, B. S. 2012, PASP, 124, 700

Coughlin, J. L., et al. 2016, ApJS, 224, 12

CRC Handbook. 2011, CRC Handbook of Chemistry and Physics, 92nd Edition

Croll, B., et al. 2014, ApJ, 786, 100

Dawson, R. I., & Fabrycky, D. C. 2010, ApJ, 722, 937

Deming, D., Seager, S., Richardson, L. J., & Harrington, J. 2005, Nature, 434, 740

Demory, B.-O., Gillon, M., Seager, S., Benneke, B., Deming, D., & Jackson, B. 2012, ApJL, 751, L28

Deroo, P., Swain, M. R., & Green, R. O. 2012, in Society of Photo-Optical Instrumentation Engineers (SPIE) Conference Series, Vol. 8442, Society of Photo-Optical Instrumentation Engineers (SPIE) Conference Series

Dragomir, D., Matthews, J. M., Winn, J. N., & Rowe, J. F. 2014, in IAU Symposium, Vol. 293, IAU Symposium, ed. N. Haghighipour, 52

Dufton, P. L., & Kingston, A. E. 1989, MNRAS, 241, 209

Dumont, A.-M., Collin, S., Paletou, F., Coupé, S., Godet, O., & Pelat, D. 2003, A&A, 407, 13

Dumusque, X., et al. 2014, ApJ, 789, 154

Ehrenreich, D., et al. 2012, A&A, 547, A18

Fegley, B., & Cameron, A. G. W. 1987, Earth and Planetary Science Letters, 82, 207

Fortney, J. J., Marley, M. S., & Barnes, J. W. 2007, ApJ, 659, 1661

Fressin, F., et al. 2013, ApJ, 766, 81

Fressin, F., et al. 2011, ApJS, 197, 5

Fulton, B. J., et al. 2017, AJ, 154, 109

García Muñoz, A. 2007, Planet.Space Sci., 55, 1426

Gardner, J. P., et al. 2006, Space Sci. Rev., 123, 485

Ghiorso, M. S., & Sack, R. O. 1995, Contributions to Mineralogy and Petrology, 119, 197

Gordon, S., & McBride, B. J. 1996, NASA Reference Publication 1311

Gray, D. F. 1976, The observation and analysis of stellar photospheres

Grießmeier, J.-M., et al. 2004, A&A, 425, 753

Guillot, T. 1999, Science, 286, 72

Guillot, T. 2005, Annual Review of Earth and Planetary Sciences, 33, 493

Hatzes, A. P., et al. 2011, ApJ, 743, 75

Haynes, K., Mandell, A. M., Madhusudhan, N., Deming, D., & Knutson, H. 2015, ApJ, 806, 146

Hirsch, C. 1990, Numerical computation of internal and external flows. Vol. 2 - Computational methods for inviscid and viscous flows

Howard, A. W., et al. 2012, ApJS, 201, 15

Howard, A. W., et al. 2013, Nature, 503, 381

Hu, R., & Seager, S. 2014, ArXiv e-prints

Hubeny, I. 2001, in Astronomical Society of the Pacific Conference Series, Vol. 247, Spectroscopic Challenges of Photoionized Plasmas, ed. G. Ferland & D. W. Savin, 197

Ida, S., & Lin, D. N. C. 2004, ApJ, 604, 388

Igenbergs, K., Schweinzer, J., Bray, I., Bridi, D., & Aumayr, F. 2008, Atomic Data and Nuclear Data Tables, 94, 981

Ikoma, M., & Hori, Y. 2012, ApJ, 753, 66

Irons, F. E. 1978, MNRAS, 182, 705

Irwin, A. W. 1981, ApJS, 45, 621

Ito, Y., Ikoma, M., Kawahara, H., Nagahara, H., Kawashima, Y., & Nakamoto, T. 2015, ApJ, 801, 144

Jin, S., & Mordasini, C. 2017, ArXiv e-prints

Kaastra, J. S., & Mewe, R. 1993, A&AS, 97, 443

Kasting, J. F., & Pollack, J. B. 1983, Icarus, 53, 479

Kawahara, H., Hirano, T., Kurosaki, K., Ito, Y., & Ikoma, M. 2013, ApJL, 776, L6

Kawahara, H., Murakami, N., Matsuo, T., & Kotani, T. 2014, ApJS, 212, 27

Kennedy, C. A., & Carpenter, M. H. 2003, Applied Numerical Mathematics, 44, 139

Koskinen, T. T., Aylward, A. D., Smith, C. G. A., & Miller, S. 2007, ApJ, 661, 515

Kreidberg, L., et al. 2014, Nature, 505, 69

Kuntz, M. 1997, J. Quant. Spec. Radiat. Transf., 57, 819

Kurucz, R. L. 1992, Rev. Mexicana Astron. Astrofis., 23, 45

Kurucz, R. L., & Avrett, E. H. 1981, SAO Special Report, 391

Kwan, J., & Krolik, J. H. 1981, ApJ, 250, 478

Lammer, H., Selsis, F., Ribas, I., Guinan, E. F., Bauer, S. J., & Weiss, W. W. 2003, ApJL, 598, L121

Lecavelier Des Etangs, A., Pont, F., Vidal-Madjar, A., & Sing, D. 2008, A&A, 481, L83

Léger, A., et al. 2009, A&A, 506, 287

Lennon, D. J., & Burke, V. M. 1994, A&AS, 103, 273

Liang, G. Y., Badnell, N. R., & Zhao, G. 2012, A&A, 547, A87

Liang, G. Y., Whiteford, A. D., & Badnell, N. R. 2009, Journal of Physics B Atomic Molecular Physics, 42, 225002

Line, M. R., Zhang, X., Vasisht, G., Natraj, V., Chen, P., & Yung, Y. L. 2012, ApJ, 749, 93

Madhusudhan, N., & Seager, S. 2011, ApJ, 729, 41

Mayor, M., & Queloz, D. 1995, Nature, 378, 355

McDonough, & Sun. 1995, Chem. Geol., 120, 223

Merle, T., Thévenin, F., & Zatsarinny, O. 2015, A&A, 577, A113

Miguel, Y., Kaltenegger, L., Fegley, B., & Schaefer, L. 2011, ApJL, 742, L19

Miller-Ricci, E., & Fortney, J. J. 2010, ApJL, 716, L74

Mordasini, C., Alibert, Y., & Benz, W. 2009, A&A, 501, 1139

Murray-Clay, R. A., Chiang, E. I., & Murray, N. 2009, ApJ, 693, 23

Neale, L., Miller, S., & Tennyson, J. 1996, ApJ, 464, 516

Nelson, B. E., Ford, E. B., Wright, J. T., Fischer, D. A., von Braun, K., Howard, A. W., Payne, M. J., & Dindar, S. 2014, MNRAS, 441, 442

Owen, J. E., & Wu, Y. 2013, ApJ, 775, 105

Owen, J. E., & Wu, Y. 2017, ApJ, 847, 29

Parker, E. N. 1964, ApJ, 139, 72

Perez-Becker, D., & Chiang, E. 2013, MNRAS, 433, 2294

Pinsonneault, M. H., An, D., Molenda-Żakowicz, J., Chaplin, W. J., Metcalfe, T. S., & Bruntt, H. 2012, ApJS, 199, 30

Piskunov, N., & Kupka, F. 2001, ApJ, 547, 1040

Plez, B. 1998, A&A, 337, 495

Pradhan, A. K. 1976, MNRAS, 177, 31

Queloz, D., et al. 2009, A&A, 506, 303

Rappaport, S., Barclay, T., DeVore, J., Rowe., J., Sanchis-Ojeda, R., & Still, M. 2013, ArXiv e-prints

Rappaport, S., et al. 2012, ApJ, 752, 1

Redfield, S., Endl, M., Cochran, W. D., & Koesterke, L. 2008, ApJL, 673, L87

Ribas, I., Guinan, E. F., Güdel, M., & Audard, M. 2005, ApJ, 622, 680

Ricker, G. R., et al. 2010, in Bulletin of the American Astronomical Society, Vol. 42, American Astronomical Society Meeting Abstracts 215, 450.06

Ridden-Harper, A. R., et al. 2016, A&A, 593, A129

Rossi, S. C. F., Maciel, W. J., & Benevides-Soares, P. 1985, A&A, 148, 93

Rothman, L. S., et al. 2013, J. Quant. Spec. Radiat. Transf., 130, 4

Rudnick, R. L., & Gao, S. 2003, Treatise on Geochemistry, 3, 1

Rybicki, G. B. 1984, Escape probability methods 21

Rybicki, G. B., & Lightman, A. P. 1986, Radiative Processes in Astrophysics

Sanchis-Ojeda, R., et al. 2015, ApJ, 812, 112

Sanchis-Ojeda, R., Rappaport, S., Winn, J. N., Levine, A., Kotson, M. C., Latham, D. W., & Buchhave, L. A. 2013, ApJ, 774, 54

Schaefer, L., & Fegley, B. 2004, Icarus, 169, 216

Schaefer, L., & Fegley, B. 2009, ApJL, 703, L113

Schaefer, L., Lodders, K., & Fegley, B. 2012, ApJ, 755, 41

Schlawin, E., Herter, T., Zhao, M., Teske, J. K., & Chen, H. 2016, ApJ, 826, 156

Schunk, R., & Nagy, A. 2000, Ionospheres: Physics, Plasma Physics and Chemistry

Seager, S., Kuchner, M., Hier-Majumder, C. A., & Militzer, B. 2007, ApJ, 669, 1279

Seager, S., Whitney, B. A., & Sasselov, D. D. 2000, ApJ, 540, 504

Sing, D. K., et al. 2013, MNRAS, 436, 2956

Sing, D. K., et al. 2015, MNRAS, 446, 2428

Sotin, C., Grasset, O., & Mocquet, A. 2007, Icarus, 191, 337

Stevenson, D. J. 1982, Annual Review of Earth and Planetary Sciences, 10, 257

Stevenson, K. B., et al. 2010, Nature, 464, 1161

Sudarsky, D., Burrows, A., & Hubeny, I. 2003, ApJ, 588, 1121

Swain, M. R., Vasisht, G., & Tinetti, G. 2008, Nature, 452, 329

Swanson, R. C., Radespiel, R., & Turkel, E. 1998, Journal of Computational Physics, 147, 518

Swanson, R. C., & Turkel, E. 1992, Journal of Computational Physics, 101, 292

Swift, D. C., et al. 2012, ApJ, 744, 59

Tachinami, C., Ogawa, M., & Kameyama, M. 2014, Icarus, 231, 377

Tayal, S. S. 2008, ApJS, 179, 534

Terada, N., Kulikov, Y. N., Lammer, H., Lichtenegger, H. I. M., Tanaka, T., Shinagawa, H., & Zhang, T. 2009, Astrobiology, 9, 55

Tian, F., Kasting, J. F., Liu, H.-L., & Roble, R. G. 2008, Journal of Geophysical Research (Planets), 113, E05008

Tian, F., Toon, O. B., Pavlov, A. A., & De Sterck, H. 2005, ApJ, 621, 1049

Tinetti, G., et al. 2012, Experimental Astronomy, 34, 311

Tinetti, G., Deroo, P., Swain, M. R., Griffith, C. A., Vasisht, G., Brown, L. R., Burke, C., & McCullough, P. 2010, ApJL, 712, L139

Toon, O. B., McKay, C. P., Ackerman, T. P., & Santhanam, K. 1989, J. Geophys. Res., 94, 16287

Torres, G., Winn, J. N., & Holman, M. J. 2008, ApJ, 677, 1324

Traub, W. A., & Oppenheimer, B. R. 2011, Direct Imaging of Exoplanets, ed. S. Seager 111

Unsold, A. 1955, Physik der Sternatmospharen, MIT besonderer Berucksichtigung der Sonne.

Valencia, D., Ikoma, M., Guillot, T., & Nettelmann, N. 2010, A&A, 516, A20

Valencia, D., O'Connell, R. J., & Sasselov, D. 2006, Icarus, 181, 545

Valencia, D., Sasselov, D. D., & O'Connell, R. J. 2007, ApJ, 665, 1413

van Lieshout, R., Min, M., & Dominik, C. 2014, A&A, 572, A76

van Lieshout, R., et al. 2016, A&A, 596, A32

van Werkhoven, T. I. M., Brogi, M., Snellen, I. A. G., & Keller, C. U. 2014, A&A, 561, A3

Verner, D. A., & Yakovlev, D. G. 1995, A&AS, 109, 125

Vidal-Madjar, A., Lecavelier des Etangs, A., Désert, J.-M., Ballester, G. E., Ferlet, R., Hébrard, G., & Mayor, M. 2003, Nature, 422, 143

Voronov, G. S. 1997, Atomic Data and Nuclear Data Tables, 65, 1

Wagner, F. W., Sohl, F., Hussmann, H., Grott, M., & Rauer, H. 2011, Icarus, 214, 366

Waldmann, I. P., & Pascale, E. 2014, ArXiv e-prints

Waldmann, I. P., Tinetti, G., Rocchetto, M., Barton, E. J., Yurchenko, S. N., & Tennyson, J. 2015, ApJ, 802, 107

Watson, A. J., Donahue, T. M., & Walker, J. C. G. 1981, Icarus, 48, 150

William, H. P., Brian, P. F., Saul, A. T., & Vetterling, W. T. 1996, Numerical Recipes in Fortran 77: The Art of Scientific Computing

Winn, J. N., & Fabrycky, D. C. 2015, ARA&A, 53, 409

Yelle, R. V. 2004, Icarus, 170, 167

Zatsarinny, O., & Tayal, S. S. 2003, ApJS, 148, 575